Materials & Design 222 (2022) 111036

Contents lists available at ScienceDirect

Materials & Design

journal homepage: www.elsevier.com/locate/matdes

Structure-property relationships of imperfect additively manufactured lattices based on triply periodic minimal surfaces

Fabian Günther [a,b,*], Franz Hirsch [c], Stefan Pilz [d], Markus Wagner [b], Annett Gebert [d], Markus Kästner [c,e,f], Martina Zimmermann [a,b]

[a] Institute of Material Science, TU Dresden, Helmholtzstraße 7, 01069 Dresden, Germany
[b] Institute for Material and Beam Technology, Fraunhofer IWS, Winterbergstraße 28, 01277 Dresden, Germany
[c] Institute of Solid Mechanics, TU Dresden, George-Bähr-Straße 3c, 01069 Dresden, Germany
[d] Institute for Complex Material, Leibniz IFW Dresden, Helmholtzstraße 20, 01069 Dresden, Germany
[e] Dresden Center for Fatigue and Reliability, DCFR, 01062 Dresden, Germany
[f] Dresden Center for Computational Materials Science, DCMS, 01062 Dresden, Germany

HIGHLIGHTS

- Ti-42Nb alloy processed by laser powder bed fusion shows promise for bone tissue engineering.
- Surface roughness and excess material on downward facing surfaces occur process-induced in TPMS lattices.
- The as-built morphology can be numerically reconstructed using a dedicated modeling procedure.
- Simulations with the reconstructed design possess high agreement with the experimental results.
- Informed predictions for the actual structure–property relationships of any TPMS based lattice are feasible.

GRAPHICAL ABSTRACT

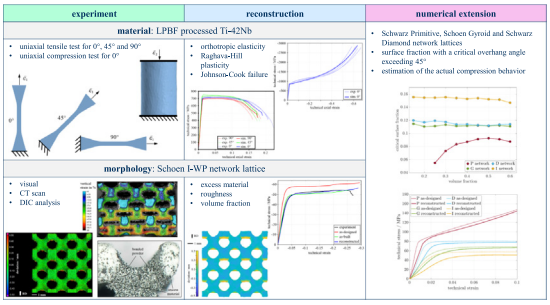

ARTICLE INFO

Article history:
Received 28 June 2022
Revised 28 July 2022
Accepted 5 August 2022
Available online 10 August 2022

2010 MSC:
00–01
99–00

Keywords:
Lattice structures
Triply periodic minimal surfaces
Additive manufacturing
Manufacturing defects

ABSTRACT

Lattices based on triply periodic minimal surfaces (TPMS) have recently attracted increasing interest, but their additive manufacturing (AM) is fraught with imperfections that compromise their structural integrity. Initial research has addressed the influence of process-induced imperfections in lattices, but so far numerical work for TPMS lattices is insufficient. Therefore, in the present study, the structure–property relationships of TPMS lattices, including their imperfections, are investigated experimentally and numerically. The main focus is on a biomimetic Schoen I-WP network lattice made of laser powder bed fusion (LPBF) processed Ti-42Nb designed for bone tissue engineering (BTE). The lattice is scanned by computed tomography (CT) and its as-built morphology is examined before a modeling procedure for artificial reconstruction is developed. The structure–property relationships are analyzed by experimental and numerical compression tests. An anisotropic elastoplastic material model is parameterized for finite element analyses (FEA). The numerical results indicates that the reconstruction of the as-built morphology decisively improves the prediction accuracy compared to the ideal design. This work highlights the

* Corresponding author at: Institute of Material Science, TU Dresden, Helmholtzstraße 7, 01069 Dresden, Germany.
E-mail address: fabian.guenther@tu-dresden.de (F. Günther).

https://doi.org/10.1016/j.matdes.2022.111036

Defect modeling
Structure–property relationship

central importance of process-related imperfections for the structure–property relationships of TPMS lattices and proposes a modeling procedure to capture their implications.

1. Introduction

Bone tissue engineering (BTE) involves the development of artificial lattices that serve as temporary or permanent replacements for injured natural bone tissue [1,2]. These biomimetic scaffolds have to meet a number of essential requirements in terms of material, design and resulting mechanical properties to ensure optimal application for the patient [3,4].

Nondegradable scaffolds from alloplastic materials are considered to be a particularly promising option for BTE. This is due to their almost unlimited availability, avoiding of disease transmission, but also because of the possibility to specifically design the morphology of the scaffolds [5,6]. Titanium and its alloys have emerged as a highly viable option due to their excellent biocompatibility and osseointegration capability. In particular, titanium-niobium alloys provide favorable properties in terms of cell adhesion and proliferation. This can be attributed to the non-toxic and non-allergenic behavior of niobium in the patient's body as well as the reduction of the Young's modulus at sufficient strength in compounds with titanium [7,8]. The reduction in elastic modulus reduces the stress-shielding effect, in which an excessively stiff implant suppresses mechanical stimulation of bone tissue and thus its proper regrowth [9,10].

Numerous studies investigating the relationship between the design and the resulting performance of the implant have revealed the eminent impact of the mesostructure in the dimension of a few hundred micrometers. Biomimetic scaffolds without a cortical-like reinforcement have been proven to be superior for osseointegration, although natural bone typically exhibits such a shell. Therefore, the use of trabecular-like lattice structures is recommended, provided that the mechanical requirements are fulfilled [11,12]. For such lattices, volume fractions around 0.3 and pores of $300 - 600\,\mu$m size are reported to be particularly well accepted by human tissue [13–15]. From a structural mechanics point of view, decreasing the volume fraction leads to an exponential decrease in the elastic structural stiffness, which again reduces the stress-shielding effect [16]. Furthermore, pore shape and surface curvature are important: due to their attractive effect on cells, concave surfaces support cell migration and thus tissue growth [17–19].

Nowadays, additive manufacturing (AM) is considered as the preferred manufacturing method for porous bone implants, as its layer-by-layer process allows the fabrication of complex CAD-designed structures [20,21]. One AM technique is laser powder bed fusion (LPBF), often named as selective laser melting (SLM), where metallic powder is selectively melted using a laser beam as energy source to build up the structure layer-by-layer. LPBF allows the manufacturing of lattices with strut size of a few hundred micrometers in a reasonable quality [22,23].

Nevertheless, manufacturing deviations are inevitable, especially for filigree and small-scale lattices. Commonly, external and internal imperfections are distinguished: while the first class includes all morphological inaccuracies such as dimensional and shape changes, the second class refers to defects within the microstructure, such as voids or cracks [24,25]. In addition, imperfections are generally associated with deviations in the target volume fraction. External imperfections have been found to be often critical to failure, especially in the case of fatigue failure. This can be attributed not least to the fact that the influence of internal imperfections can be substantially reduced in a practical way by suitable post-treatment compared to external imperfections [26,27]. Anyway, since lattice imperfections have a decisive influence on performance and premature failure on the one hand, but are insufficiently understood and controllable on the other hand, they are rarely used in engineering applications [28–31].

Lattice structures based on triply periodic minimal surfaces (TPMS) have attracted particular attention in BTE [32–35]. This lattice class has also been studied in other engineering applications, such as the construction [36,37], electrical [38], acoustic [39], transportation [40], chemical [41], optical [42], and energy [43,44] industry. The keen interest in TPMS based lattices is explained by the variety of exceptional characteristics, including the control of the pore size, strut size, curvature and volume fraction [45–47], the ability of functional grading [48–50], the high surface area at low volume fraction [51,52], the high strength combined with low stiffness [53], and the good fluid dynamic characteristics [54–56]. Moreover, numerous studies have demonstrated that the structure–property relationships of TPMS lattices can be numerically captured in principle by computational solid mechanics [57,58] and computational fluid dynamics (CFD) [59,60].

Nevertheless, there are often discrepancies between numerical results and actual behavior, since the used CAD models represent an idealized as-designed state, while the experiment is performed with the as-built state including all imperfections [61,62]. Due to their novelty and challenging fabrication, TPMS lattices are particularly prone to nonconformities [30,63,64]. To overcome the as-built/as-designed mismatch, first approaches for simulative evaluation and prediction of manufacturing defects have been reported in recent years. Gebhardt et al. [65] derived a finite element material model from mechanical tests on bulk specimens, which could be used to predict the behavior of complex strut-based lattices. Zhang et al. [66] simulated lattice structures with adjusted volume fractions, so that the numerical results agreed well with the experiment. In order to investigate the influence of imperfections in the microstructure on the fatigue behavior of AM processed components, Bonneric et al. [67] introduced artificial pores into the specimens. In this way, the researchers were able to evaluate the criticality of the pores depending on their position and finally to predict the fatigue behavior by simulation.

Another frequently applied method for accessing the structure–property relationships is the exploitation of computed tomography (CT) scans. Accordingly, Amani et al. [68] derived heterogeneous models from CT scans of lattice structures and predicted the fracture location using finite element analysis (FEA). Raßloff et al. [69] presented a numerical method to capture the microstructure with pores from CT scans and statistically analyze. On this basis, representative volume elements were modeled that allow the prediction of the fatigue behavior using FEA. Dallago et at. [70] performed FEA based on the CT data and achieved good agreement between the measured and simulated stiffness. In a subsequent study, the authors also succeed in estimating the fatigue behavior of AM processed lattices with CT data [71]. Liu et al. [23] numerically predicted the compressive stiffness and strength of LPBF fabricated lattices based on CT scans.

Although the abovementioned methods generally provide good agreement with experimental results, they only allow simulations for already fabricated lattices. In particular, the process of defect insertion remains uncertain, preventing the transfer to other AM lattice structures. Lozanovski et al. [72,73] have begun to solve this drawback for strut-based trusses through a modeling approach in which characteristic morphological design features were derived from CT scans. Once design parameters were specified, the as-built morphology of other conventional trusses as well as their mechanical properties could be predicted.

However, there is a lack of reconstruction methods for TPMS based lattices so far. This is a major reason why their structure integrity cannot yet be sufficiently ensured for extensive technical use. This is particularly true for BTE, where high safety requirements and conflicting design criteria still often preclude clinical use. In order to unlock the enormous potential of TPMS lattices for seminal high-performance applications, modeling concepts for reconstructing the as-built morphology are required. In the present study, such a modeling procedure is proposed: insights into the actual structure–property relationships of TPMS lattices can be obtained by artificially introducing imperfections. In particular, the distinctive AM mesostructure is reconstructed independently, instead of using a one-to-one adaptation from CT data. This is critical because in practice CT data are often not available due to component dimensions and effort. Over the longer term, characteristic modeling parameters for different TPMS lattices and LPBF process parameters should be derived to predict the structural properties nondestructively and without high-quality instrumentation.

Specifically, the study includes the following: firstly, a Ti-42Nb biomimetic lattice based on the Schoen I-WP network TPMS with a volume fraction of 0.27 designed for BTE is fabricated by LPBF. Using CT scans and uniaxial compression tests, this lattice is characterized experimentally. Secondly, an anisotropic elastoplastic material model corresponding to additively processed Ti-42Nb is parameterized for FEA. The required material properties are obtained by uniaxial tensile and compression tests on bulk specimens. Thirdly, a procedure to reconstruct as-built state of TPMS lattices is presented. The suitability of the approach is evaluated both morphologically and mechanically: the numerical results of the as-designed, the as-built, and the reconstructed I-WP lattice are compared with those of the fabricated lattice. Fourthly, the transferability of the proposed modeling approach to further common TPMS based lattices is discussed.

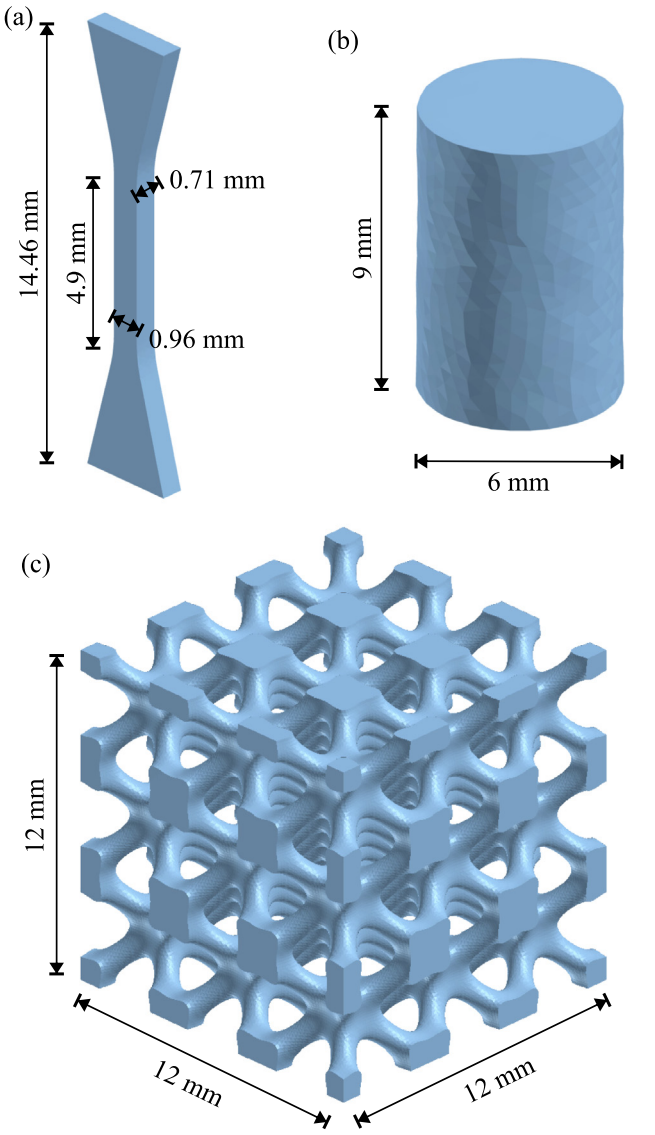

Fig. 1. Visualization of fabricated specimens: in (a) the tensile specimens are shown, in (b) the compression specimens, and in (c) the Schoen I-WP (I) network lattice with 0.27 volume fraction and a unit cell size of 4 mm.

2. Methods

In this section, the experimental and numerical procedures are outlined. In Section 2.1, the experimental details, including material, design, fabrication, and testing of the specimens are explained. Subsequently, the modeling procedure of the as-built TPMS lattice is described in Section 2.2 before the FE modeling concludes this section in Section 2.3.

2.1. Experimental work

The geometries of the bulk specimens are shown in Fig. 1(a) and (b). A total of nine tensile specimens with rectangular cross-sections and five cylindrical compression specimens were extracted from 9 mm x 19 mm x 40 mm large cuboids by electric discharge machining (EDM). The tensile specimens were extracted parallel (0°), perpendicular (90°), and at a 45° angle to the building direction (BD). Thus, three tensile specimens were analyzed for each testing directions to capture the manufacturing-related anisotropy of the material properties. The compression specimens were in the 0° configuration.

The considered lattice is based on the Schoen I-WP (I) network TPMS with 3 x 3 x 3 unit cells, a volume fraction of 0.27 and a unit cell size of 4 mm. Here, unit cell denotes the minimum of the lattice that can be periodically continued. In Fig. 1(c), the lattice design is illustrated. In the previous work [3], this lattice type has been found to be favorable for human bone tissue consisting of Ti-42Nb, especially for trabecular bone. To obtain its mesh in STL-file format based on its level set function ϕ, MATLAB software (MathWorks, Natick, USA) was used. The procedure was previously detailed in [3].

All specimens were additively manufactured from biocompatible Ti-42Nb alloy. The pre-alloyed, gas-atomized Ti-42Nb powder used was supplied by TANIOBIS GmbH (Goslar, Germany) [74]. The chemical composition of the Ti-42Nb powder was determined by inductively coupled plasma optical emission spectrometry (ICP-OES) and carrier gas hot extraction (LECO TC-436DR). The distribution of particle size was also measured. More details can be found in [75].

A SLM 280 Generation 2.0 dual-laser machine (SLM Solutions Group AG, Germany) equipped with an infrared laser source with

Gaussian beam profile and 80 μm beam size was used to fabricate the specimens. The process parameters for the specimens were calibrated by a previously performed optimization procedure, cf. [75]. For the bulk specimens, a laser power of 250 W, a scanning speed of 1000 mm/s, a hatch distance of 100 μm, and a layer thickness of 50 μm was used. For the lattice, the laser power as well as the scanning speed were reduced to 150 W and 650 mm/s, respectively. Furthermore, a scan rotation of 67° was employed for both specimen types. The extent to which the investigation is reasonable due to the different process parameter sets and specimen dimensions is discussed in Section 3.

A GE Phoenix Nanotom M (Waygate Technologies, Wunstorf, Germany) was employed for micro-CT scans with a resolution of 9.5 μm at 140 V voltage and 120 μA current. The volume reconstruction from CT scans was performed with Phoenix datosx 2.2 software (Baker Hughes, Houston, USA) and VG-studio max 3.5 software (Volume Graphics, Heidelberg, Germany) was used for analysis. The material density of the bulk specimens was measured on mechanically and chemically polished cross sections with a digital microscope (VHX7000, Keyence Deutschland GmbH, Germany). The relative volume fraction of the lattice was determined with CT scans.

A hydraulic universal test bench (Instron® GmbH, Germany) with a load cell for 50 kN and a displacement rate of 0.04 mm/s was employed for the uniaxial compression tests. To transfer the load from the frame to the specimen, the machine was equipped with plane-parallel stainless steel anvils. The uniaxial tensile tests were performed using a tensile-compression module (Kammrath & Weiss GmbH, Germany) with a displacement rate of 0.00175 mm/s and a 5 kN load cell.

The displacement was measured optically with a microDAC video extensometer and the strain was subsequently evaluated with VEDDAC strain software (Chemnitzer Werkstoffmechanik GmbH, Germany). The reference length for calculating the axial strain of the tensile specimens was 4.9 mm mm, whereas 0.96 mm mm was used for the in-plane transverse strain. For the latter, the necking point was considered. VEDDAC 7 software was employed to evaluate the strain distribution of the lattice by means of digital image correlation (DIC). For video recording, a Nikon D7100 camera (Nikon, Japan) with a SIGMA DG Macro HSM 105 mm objective (Sigma Corporation, Japan) was used.

For material characterization, the individual test results were averaged. In this way, statistical effects were reduced, while generally good repeatability was found for all tests. The specified mechanical quantities include both the average and the standard deviation. In contrast, no statistical validation was performed for the characterization of the lattice due to the limited specimen number.

2.2. Modeling of as-built TPMS lattices

Additively manufactured TPMS lattices exhibit surface roughness as well as missizing of faces, struts and nodes (see Section 1). While the former type is typically homogeneously distributed throughout the structure, the latter effect occurs mainly at downward facing surfaces. In the following, a semi-random multi-step modeling procedure is presented, in which the as-built state of lattices is reconstructed independently and not taken one-to-one from CT scans. For distinction, the ideal CAD lattice is called as-designed model in this study, the lattice derived immediately from CT data is called as-built model, and the lattice obtained by the modeling procedure is called reconstructed model. In Fig. 2 an example is shown for each type.

Since the general modeling of TPMS lattices has already been described in the literature (cf. [3,64]), only the specifics are detailed here. The starting point is the ideal TPMS in STL-file format, determined by its level set function ϕ and the level set constant r for the desired volume fraction. Here, the target value for the volume fraction of the as-designed and the reconstructed lattices is the volume fraction of the as-built lattice obtained by CT measurement. The modeling procedure then rearranges the surface in three steps, where the z-direction is assumed to be the BD.

In the first step, excess material is added to the downward facing surfaces. For this, the slope of the lattice is required. Due to the implicit description of TPMS, this is done analytically by determining the gradient of the level set function $\nabla\phi$ with respect to the three spatial directions x, y and z. Subsequently, the angle θ that the gradient encloses with the base vector in z-direction e_z is computed by means of the relation

$$\theta = \arccos\left(\frac{\nabla\phi \cdot e_z}{|\nabla\phi|}\right). \tag{1}$$

Based on the angle θ, an empirical function $g_1(\theta)$ is defined. The function is added to the z-coordinate of each surface node of the as-designed model. A sigmoid function is used to ensure continuity according to

$$g_1(\theta) := C_3 + \frac{C_4 - C_3}{1 + \exp\left(C_1(C_2 - \theta)\right)}. \tag{2}$$

The parameters C_1 to C_4 control the characteristic of the function: C_1 adjusts the slope of the function, C_2 defines the inflection point, and C_3 and C_4 are the upper and lower asymptotes.

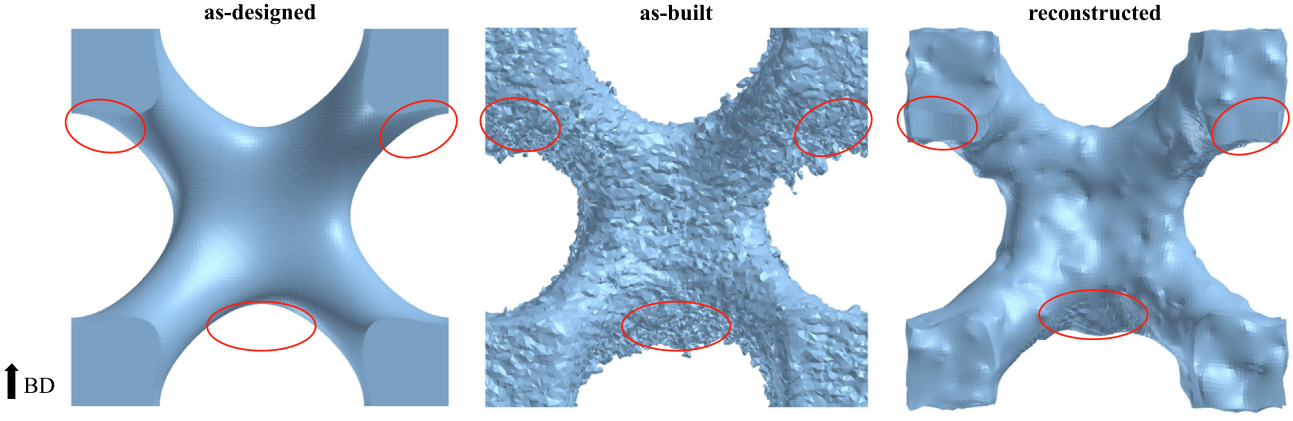

Fig. 2. Side view of a unit cell in as-designed, as-built and reconstructed configuration. The reconstruction is created following the procedure described in Section 2.2. The building direction (BD) is upward. Highlighted are downward facing surfaces where process-induced excess material occurs in reality.

After adding the material excess on downward facing surfaces, the roughness is applied in the second step. For this purpose, the surface is shifted heterogeneously, i.e. with random magnitude and direction. In particular, an iteration loop is executed, where each iteration slightly edits the surface. Here, one iteration comprises the following: a point and a direction are randomly defined within the $(12\,\mathrm{mm})^3$ large design space of the 3 x 3 x 3 unit cell lattice. From these two quantities, a position-dependent shift vector is calculated for each surface node, which is added to its coordinates. While the direction remains constant for each node, the magnitude depends on the distance d between the defined random point and the surface node. A second empirical function $g_2(d)$ serves here as a scaling function. In order to achieve a continuous and spatially limited impact of each iteration, a decaying exponential function is used according to

$$g_2(d) := C_5 \exp(-C_6\, d). \tag{3}$$

Parameter C_5 measures the maximal shift of a surface node per iteration and C_6 determines the influence range. The described surface modification is looped 54000 times, which corresponds to 2000 iterations per unit cell.

After these two modeling steps, the as-built morphology is essentially reconstructed. However, the modifications are accompanied by changes in the volume fraction. Therefore, in the third step, the level set constant r is readjusted to drive the volume fraction to the target value, i.e., the volume fraction of the CT scan.

The parameter calibration is done manually based on the as-built lattice. The level set constant r is chosen so that the reconstructed model has the same volume fraction as the as-built model. The further parameters C_1 to C_6 of the modeling functions g_1 and g_2 are tuned simultaneously to minimize the objective variable. In this study, the Boolean difference volume between the as-built model and the reconstructed model is used as objective variable. This indicator explicitly captures the morphology of the lattices, which is crucial since the volume fraction remains constant in all simulations and is therefore not meaningful. The measurement is accomplished with nTopology software (nTopology, New York City, USA).

It is worth mentioning that the stochastic type of modeling does not provide a unique lattice design: although the basic structure of the lattice with the excess material persists, the final design varies due to the randomly distributed surface roughness. To verify the reproducibility of this semi-random modeling procedure, the parameterization is performed for a statistically significant number of lattices and the resulting scatter is measured. In particular, the considered number ensures that the normalized Boolean difference volume is within the confidence interval to the 95% level.

2.3. Finite element modeling

In this section, the methods of FE modeling are outlined. The FEAs are performed with Pam-Crash software (ESI Group, Paris, France). All models are solved using the explicit solver. In order to obtain tetrahedron volume meshes, the triangular surface mesh of the idealization, the as-built model and the reconstructed model are edited using nTopology software. Quadratic shape functions (i.e., TETRA10 elements) are applied. The number of elements required for sufficient accuracy is identified by h-refinement mesh studies prior to further simulations. Starting from the original CT scan with 1.87kk surface elements, the approximation quality of the as-built model is reduced until the technical stress–strain curve from a compression test converges to 1% tolerance. The identified mesh parameters (i.e., target element size and minimum feature size,) are applied to each calculation.

In addition to meshing, the significance of the simulation results in terms of reproducibility is important. This is particularly relevant for the semi-random modeling procedure from Section 2.2. Therefore, reproducibility is analyzed based on ten calculations with identically parameterized reconstructed models.

A material model is parameterized that reflects the uniaxial behavior of LPBF processed Ti-42Nb from tensile and compression tests of the bulk material. The averaged stiffnesses and strengths as well as the density from material characterization are used as a reference. The material model includes orthotropic elasticity as well as anisotropic plasticity. For the latter, besides anisotropic onset of plastic yielding and isotropic strain hardening, a tension–compression anisotropy at failure is considered.

The elastic material behavior is determined by nine parameters: the elastic moduli E_i, the shear moduli G_{ij} and the Poisson's ratios ν_{ij}, with $i, j = 1, 2, 3$. The three orthotropic axes correspond to the three spatial directions x, y and z, where the z-direction represents the BD.

The directional onset of plastic flow is described by the Raghava-Hill plasticity model [76–78], which combines an anisotropic yield function with a tension–compression asymmetry. The yield function reads

$$f(\boldsymbol{\sigma}, \alpha, R) = \frac{3(\alpha-1)\,\sigma_\mathrm{m} + \sqrt{9((\alpha-1)\,\sigma_\mathrm{m})^2 + 4\alpha\,\sigma_\mathrm{H}^2}}{2\alpha} - R. \tag{4}$$

Here, $\sigma_\mathrm{m} = \mathrm{tr}(\boldsymbol{\sigma})/3$ denotes the hydrostatic stress of the Cauchy stress tensor $\boldsymbol{\sigma}$, and R represents the current yield stress. Parameter $\alpha = \sigma_\mathrm{y}^\mathrm{c}/\sigma_\mathrm{y}^\mathrm{t}$ measures the compression-tension ratio of the initial yield stress in compression $\sigma_\mathrm{y}^\mathrm{c}$ and tension $\sigma_\mathrm{y}^\mathrm{t}$. The effective Hill stress σ_H is defined by

$$\begin{aligned}\sigma_H = {} & F(\sigma_{yy}-\sigma_{zz})^2 + G(\sigma_{zz}-\sigma_{xx})^2 + H(\sigma_{xx}-\sigma_{yy})^2 + 2L\sigma_{yz}^2 \\ & + 2M\sigma_{zx}^2 + 2N\sigma_{xy}^2,\end{aligned} \tag{5}$$

where F, G, H, L, M and N are constants describing the directionality of the yield function.

Strain hardening is captured by a power law model according to

$$\sigma(\varepsilon_\mathrm{p}) = \min(a + b\,\varepsilon_\mathrm{p}^n,\, \sigma_\mathrm{max}), \tag{6}$$

where a represents the initial yield stress, b the strain hardening coefficient, n the strain hardening exponent and σ_max the maximum permissible stress. ε_p denotes the effective plastic strain, which is calculated with the plastic deformation rate tensor D^p at time t by

$$\varepsilon_\mathrm{p} = \int_0^t \sqrt{\frac{2}{3} D_{ij}^\mathrm{p} D_{ij}^\mathrm{p}}\,\mathrm{d}t. \tag{7}$$

Finally, the Johnson–Cook (JC) damage criterion is used to describe the onset of material failure [79]. The JC damage criterion is a strain-rate dependent empirical model that incorporates the weighted accumulation of local plastic strain for determining the damage initiation variable D_int. Damage initiates at

$$D_\mathrm{int} = \sum \frac{\Delta\varepsilon_\mathrm{p}}{\varepsilon_f} = 1, \tag{8}$$

where ε_f denotes a weighting function. This function considers the stress triaxiality $\eta = \sigma_{ii}/\sigma_\mathrm{eq}$, the equivalent stress $\sigma_\mathrm{eq} = \sqrt{3/2\,\sigma_{ij}\sigma_{ij}}$ as well as the effective plastic strain rate $\dot{\varepsilon}_\mathrm{p}$ according to

$$\varepsilon_f = \left(D_1 + D_2 \exp\left(-D_3 \frac{\eta}{3}\right)\right)\left(1 + D_4 \ln\left(\frac{\dot{\varepsilon}_\mathrm{p}}{\dot{\varepsilon}_0}\right)\right). \tag{9}$$

The model parameters D_1 to D_4 have to be adjusted to the observed material behavior. Damage evolution is described by an abrupt failure progress involving element elimination when the onset of damage is attained.

The boundary conditions of all different FE models are illustrated in Fig. 3. The displacement-controlled loads of the simulation are converted here to their corresponding technical strains for interpretability. For tensile specimens, all degrees of freedom of one side are constrained and on the other side the axial technical strain $\bar{\varepsilon}_1 = 0.1$ is applied. Analogous to the experiment, the $0^\circ, 45^\circ$ and 90° orientation to the BD are considered separately. During loading, the reaction force at the restrained side, the displacement of the parallel 4.9 mm long shaft, and the cross-sectional area at the necking location are measured.

For the compression tests, rigid plates are modeled immediately at the upper and lower side of the specimens and provided with a surface-to-surface contact condition. The friction coefficient is set to 0.3 to reflect the experimentally observed motion at the interfaces. Moreover, self-penetration of the specimens is excluded by an additional contact condition. While all degrees of freedom of the lower plate are constrained, only vertical displacement is allowed at the upper plate. For the bulk specimens, the axial technical strain $\bar{\varepsilon}_2 = -0.6$ is applied at the upper plate, and for the lattices $\bar{\varepsilon}_3 = -0.3$. The reaction force and displacement of the plate are measured during the compression tests.

In this study, technical axial and transverse strains are calculated by relating the respective displacement to the initial length, and technical stresses by relating the force to the initial cross-sectional area. In addition, the initial range of technical stress–strain curves is prepared by extending the elastic straight line tangentially and using the intersection with the strain axis as the starting point. The characteristic mechanical parameters such as stiffness and strength are measured according to the method described by Ma et al. in [55].

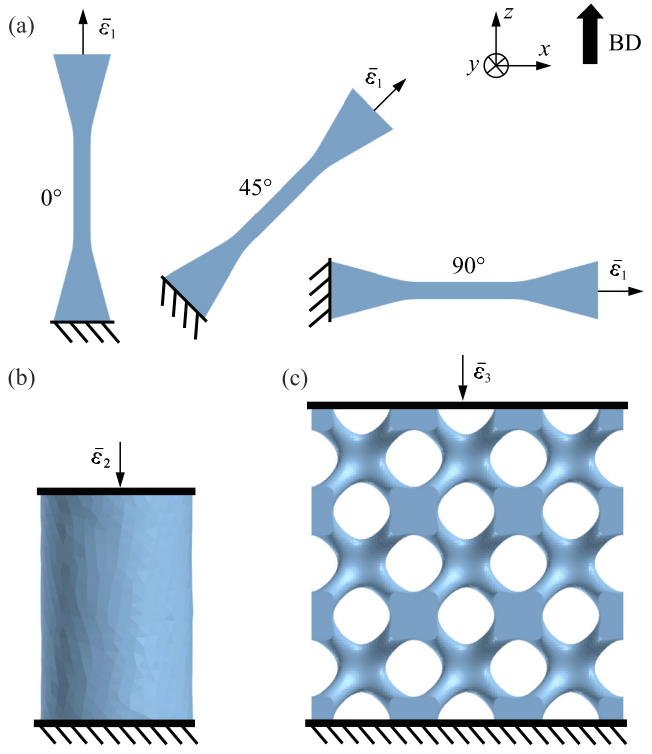

Fig. 3. Boundary conditions (a) for the tensile specimens with an applied technical strain of $\bar{\varepsilon}_1 = 0.1$, (b) for the bulk compression specimens of $\bar{\varepsilon}_2 = -0.6$, and (c) for the lattices of $\bar{\varepsilon}_3 = -0.3$.

Table 1
Chemical composition of pre-alloyed, gas-atomized Ti-42Nb powder used for LPBF processing.

element	Ti	Nb	O
wt.%	57.9 ± 0.33	41.49 ± 0.25	0.285 ± 0.001

3. Results and discussion

In the following section, the experimental and numerical results are presented and analyzed. In Section 3.1, the mechanical properties of the bulk material from experiments and simulations are evaluated, and in Section 3.2, the morphology of the fabricated and modeled lattice is investigated. In Section 3.3, the structure–property relationships of the I-WP lattice are discussed before Section 3.4 concludes this section with a numerical extension of the modeling procedure to additional TPMS lattices.

3.1. Mechanical properties of the bulk specimens

In this section, both experimental and numerical mechanical results of the LPBF processed Ti-42Nb bulk specimens are studied. The chemical composition of the powder was determined in the previous work [75] and is listed in Table 1. This shows good agreement with the nominal composition of the alloy. Even though the composition was not measured after processing, the inert gas atmosphere suggests that the deviation is marginal. The particle size ranges from $10 - 63\,\mu$m and the percentiles are $d_{0.1} = 17\,\mu$m, $d_{0.5} = 30\,\mu$m and $d_{0.9} = 51\,\mu$m. The material density of the processed specimens is equal to $5.64\,\mathrm{g/cm^3}$, or 99.94%. Further details on microstructure can be found in [75]. Here, only the comparatively low dependence of the microstructure on the BD should be emphasized.

The graphical results of the experiments for mechanical characterization are shown in Fig. 4. Both the technical stress–strain curves in (a) and the technical in-plane transverse strains at the necking point in (b) of the uniaxial tension tests include the three extracting directions $0^\circ, 45^\circ$, and 90°. The technical stress–strain curves of the uniaxial compression tests in (c) are for the 0° direction. Table 2 contains the corresponding average values and standard deviations. Here, the directional stiffness E, the yield stress σ_{YS} and the ultimate tensile stress σ_{UTS} are presented for tensile loading. For compressive loading, the compressive yield stress $\sigma_{c0.2}$ and the compressive stress at -0.3 axial technical strain σ_{c30} are listed.

Essentially, the experimental results for the mechanical properties of LPBF processed Ti-42Nb agree well with those reported in the literature [75,80], although the values depend on the process parameters. Characteristic of Ti-Nb alloys is the pronounced plateau-like stress–strain relationship with plateau stress in the plastic regime. The additively manufactured variant exhibits excellent strength and ductility values compared to other manufacturing processes, such as cast and solution annealed [81,82]. In the present study, the high elongations at fracture above 15% for all extraction directions can be particularly highlighted.

The identified material parameters of the FE material model are listed in Table 3. The corresponding simulation results are presented in Fig. 4 and Table 2 together with those of the experiments. The comparison indicates that the parameterized material model is suitable: besides the anisotropic material behavior of LPBF processed Ti-42Nb under tensile load, the compressive behavior is captured. Due to the moderate anisotropy, an isotropic FE material model could be used to simplify the parameterisatzion. At least for the elastic behavior, no major influence is to be expected. Furthermore, it is worth noting that the abrupt element elimination

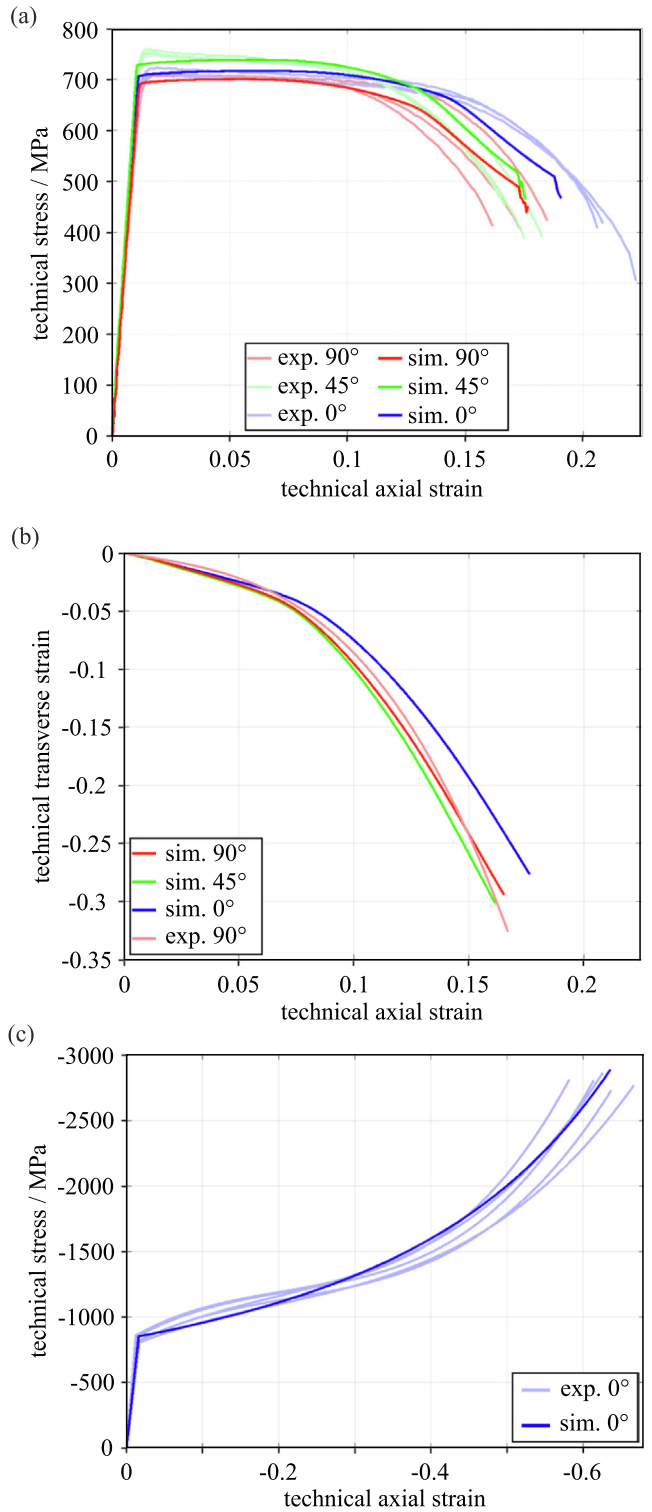

Fig. 4. Experimental and numerical results of uniaxile mechanical characterization of LPFB processed Ti-42Nb: technical stress–strain curves for tensile tests are shown in (a), the corresponding technical in-plane transverse strains at the necking point in (b), and the technical stress–strain curves for compression tests in (c).

proves to be effective when the JC damage criterion is reached. In fact, failure occurs only at the end of the tensile tests, while no damage or failure occurs during the compression tests. Finally, as Fig. 4(a) and (b) illustrate, both the technical stress–strain curves and the deformation process, including necking, are essentially reflected.

However, it remains uncertain to what extent the technical in-plane transverse strain at the necking point is representative of the actual spatial strain. The same is true for the parameterization of JC damage model: firstly, only the tension–compression anisotropy is taken into account, but no further directional dependencies. Secondly, the damage model was parameterized with respect to the primarily uniaxial load cases in tension and compression testing. It is questionable whether this parameterization is sufficient to properly describe multiaxial stress states. This could be a critical drawback for further numerical work on lattice structures as they involve multiaxial stress states. This topic is addressed in Section 3.3, among others.

3.2. Morphology of the lattice

In this section, the morphology of the fabricated and modeled lattices is examined and compared. Fig. 5(a) shows light microscope images of the LPBF processed I network lattice with 3 x 3 x 3 unit cells of 4 mm size and 0.27 volume fraction. The specific TPMS morphology is essentially well represented, but morphological mismatches due to missizing and surface roughness are observed.

Without quantification, it can be stated that no roughness patterns are visible on the lattice. Furthermore, the comparison between top view and side view discloses a comparatively minor directional dependency. Therefore, an approximately homogeneous roughness can be assumed. For more informative statements, the surface roughness parameters would be required. In the magnified view, bonded powder particles are visible on the lattice causing the surface roughness. This phenomenon is traceable to the LPBF process and was already discussed in other studies [36,83,84]. However, preclinical studies on osseointegration have shown that rough surfaces resulting from the AM process can facilitate cell attachment and ingrowth [85,86]. In contrast to roughness, missizing occurs primarily locally on downward facing surface, as indicated by the equally sized red circles in the top and side views. The deviation is opposite to the BD, effectively resulting in excess material. The cause of this local concentration is the direction-dependent heat conduction during the layer-by-layer manufacturing process and the resulting overheating. Effectively, this leads to dross formation and partial melting of loose, unsupported powder on downward facing surface. The material adherence increases the as-built volume fraction compared to as-designed. Accordingly, the volume fraction of 0.292 determined in the CT scan exceeds the target value of 0.27.

Using the as-built/as-designed comparison in Fig. 5(b) and (c) proposed by CT data, the morphological mismatch can be quantified: 90% of the surface exhibits deviations less than or equal to ±0.1 mm, tending to be surface roughness. The remaining 10% of the surface have predominantly larger positive deviations of up to 0.5 mm. In particular, this is indicated by the two separate portions within the deviation distribution in Fig. 5(c): firstly, a normally distributed portion correlated with roughness, and secondly, an smaller portion in the positive deviation region due to excess material.

The same is reflected in the CT images in Fig. 5(d) and (e): with the given resolution, no distinct preferred directions or patterns of roughness are apparent either in a single view or when comparing side and front views. In terms of magnitude, this predominantly homogeneous roughness remains below 0.1 mm. Furthermore, it is observed that surfaces with more than about 45° overhang exhibit up to 0.5 mm excess material. The determined critical overhang angle coincides with the common literature [87–89]. This local concentration of excess material induces the build direction dependency of AM processed lattices. Typically, this results in an asymmetric morphology especially in the side view, cf. Fig. 5(e).

Table 2
Mechanical properties of tensile and compression specimens from experiment and simulation for different building directions: E denotes the directional Young's modulus, σ_{YS} the yield stress and σ_{UTS} the ultimate tensile stress, and $\sigma_{c0.2}$ the compressive yield stress and σ_{c30} the compressive stress at −0.3 axial technical strain. The experimental data include the average and standard deviation.

		E / GPa	σ_{YS} / MPa	σ_{UTS} / MPa	$\sigma_{c0.2}$ / MPa	σ_{c30} / MPa
0°	experiment	64±0.5	685.67 ± 9.1832	722.98 ± 7.638	856.66 ± 38.704	1289.7 ± 38.335
	simulation	64	706.89	721.2	864.2	1307.5
45°	experiment	69.2±1.4	727.1 ± 4.4451	756.72 ± 6.0211	-	-
	simulation	69.2	738.54	747.41	-	-
90°	experiment	60±0.6	669.97 ± 2.3784	709.38 ± 3.8456	-	-
	simulation	60	693.74	698.11	-	-

Table 3
Parameters of the LPBF processed Ti-42Nb material model proposed in Section 2.3.

	parameter	value	unit
orthotropic elasticity	E_{xx}	60.0	GPa
	E_{yy}	60.0	GPa
	E_{zz}	64.0	GPa
	G_{xy}	21.5	GPa
	G_{yz}	26.0	GPa
	G_{zx}	26.0	GPa
	ν_{xy}	0.4	-
	ν_{yz}	0.4	-
	ν_{zx}	0.4	-
Raghava-Hill plasticity	F	1.2	-
	G	0.9	-
	H	1.0	-
	L	3.0	-
	M	3.0	-
	N	3.0	-
	α	1.2234	-
strain hardening	a	1000	MPa
	b	790	MPa
	n	0.8	-
	σ_{max}	1400	MPa
Johnson–Cook failure	D_1	0.75	-
	D_2	0.65	-
	D_3	10000	-
	D_4	0.0001	-

In comparison, Davoodi et al. found in [90] on LPBF-processed TPMS lattices with 2 mm unit cell size of Schwarz Primitive and Diamond type made of Ti-6Al-4 V excess material at overhanging surfaces ranging from $190 - 340\,\mu$m. These findings are consistent with those made here, as the Schoen I-WP is considered procedurally challenging, cf.[13].

The considerable morphological mismatch is expected to have a decisive effect on the mechanical performance of the lattice: under load, any imperfection in the lattice introduces stress concentrations. This ultimately results in premature failure compared to the ideal lattice. Due to own experience as well as the pertinent literature (e.g. [31,64,72]), it is to be expected that the findings are independent of the material: even with optimized process parameters, the characteristic morphological imperfections, i.e. missizing and roughness, are inherent to the PBF processes.

The identified parameters of the modeling procedure for reconstructing the as-built morphology described in Section 2.2 are listed in Table 4. Fig. 6 (a) and (b) contain the graphical representations of the parameterized modeling functions 2 and 3. Additionally, a sample geometry is illustrated for both modeling steps.

It is worth noting that the volume fraction changes during the different modeling phases: adding excess material in the first step increases the volume fraction from the original 0.292 to 0.3311. In the second step, the fraction is reduced to an average of 0.3167 by applying roughness. Then, in the third step, the target value of 0.292 is set again by readjusting the level constant r. In total, the parameterization indicator, the Boolean difference volume with respect to the as-built lattice, is reduced by the reconstruction procedure to $4.93\% \pm 0.281\%$ compared to 10.64% for the as-designed lattice. This alignment to the as-built morphology results from the multi-step modeling procedure, in which the material distribution is adjusted but not its volume.

Basically, two main implications of the material redistribution process emerge: firstly, the nodes of the lattice become thicker due to the excess material on their underside. However, since the total amount of material remains constant, secondly, the struts of the lattice become thinner in the process. In this way, potential predetermined breaking points arise, which can exert a serious impact on the structure–property relationship. This will be investigated in the next section for uniaxial compression tests.

The statistic for the absolute deviation between the as-designed and the reconstructed model in Fig. 7(a) reveals that 90% surface fraction exhibit comparatively small absolute deviations less than 0.105 mm. This deviation is overwhelmingly normally distributed, as can be seen from the directional distribution in Fig. 7(b). In addition, a larger positive deviation of up to 0.5 mm occurs at about 10% of the surface, indicating excess material. Examining the top and front views in Fig. 5(c) and (d), the deviation features can be assigned to different surface regions: the excess material occurs at downward facing surfaces, while the surface roughness is homogeneously present throughout the lattice.

Comparing the as-built and the reconstructed lattices an overall high agreement can be stated: the essential morphological features of the as-built TPMS lattice are captured by the procedure both qualitatively and quantitatively. Despite the lack of statistical validation for the as-built lattice, this general statement remains valid. Even if deviating average characteristic values should be found for a representative specimen number, this can be covered by reparameterization of the modeling parameters from Table 4. The same is true for a changed cell size, where the relative deviation would presumably be larger, but the imperfections would likely occur in a similarly systematic manner. Therefore, rescaling of the lattice should be captureable by the modeling procedure. Moreover, it is worth mentioning in this context that statistical effects are accounted by the semi-random procedure: excess material is located deterministically, whereas surface roughness is distributed randomly. Therefore, a certain variance for the final model design analogous to the real conditions is given. In this way, overfitting for a single lattice can be avoided.

Finally, the modeling procedure provides a quasi as-built morphology for further numerical structure–property investigations. Depending on the specific application, subsequent solid mechanical, fluid and thermodynamic simulations can supply valuable insights into the actual component behavior. Accordingly, in the next Section 3.3 the influence of the as-built morphology on the compression behavior is studied by FEAs.

3.3. Mechanical properties of the lattice

In the following section, the experimental and numerical mechanical properties of the I network lattice are presented and

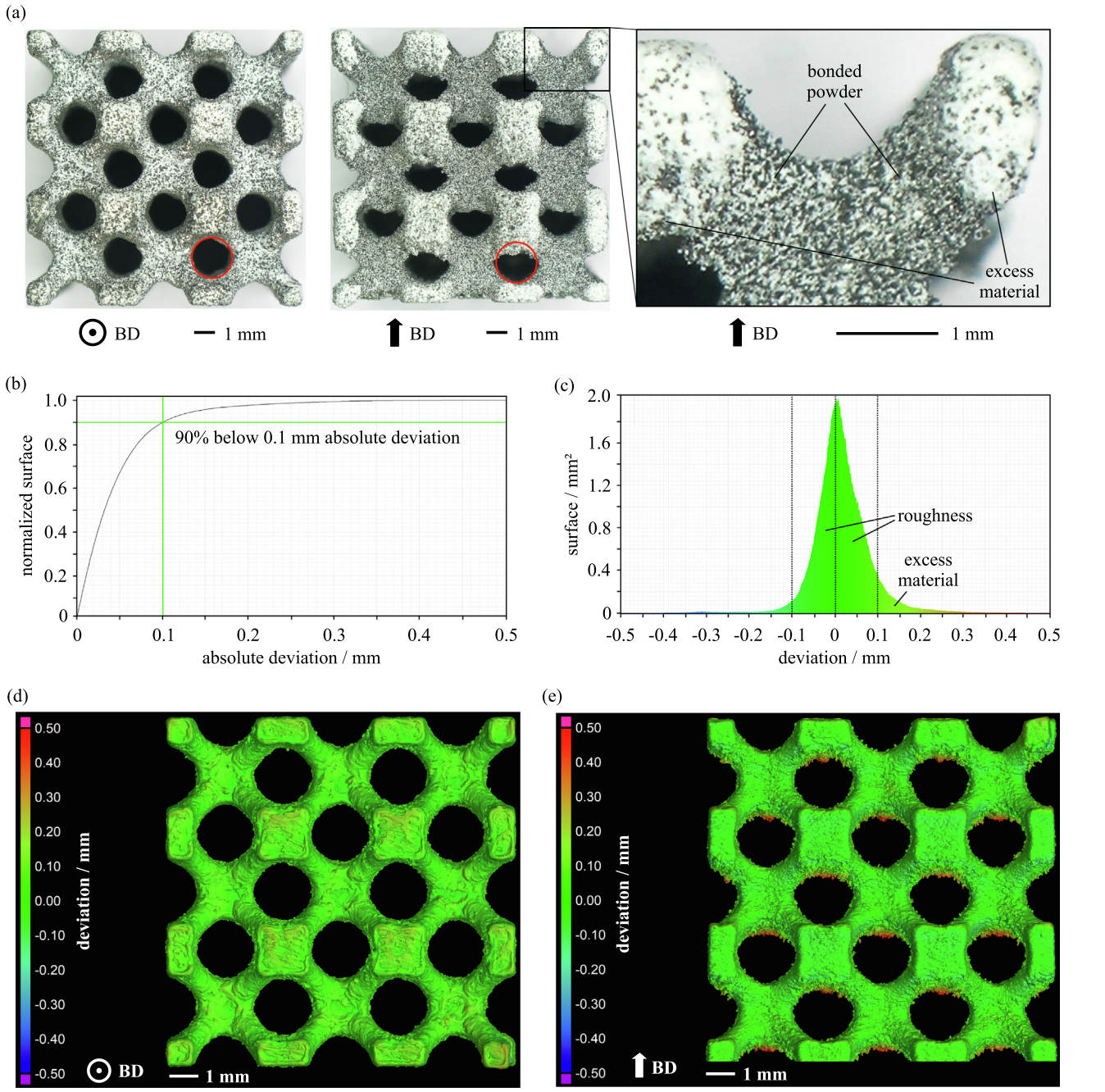

Fig. 5. Experimental data of the morphology of the 3 x 3 x 3 I network lattice with 4 mm unit cell size: (a) shows different views from light microscope, (b) and (c) display statistics to the morphological as-built/as-designed mismatch from CT data, (d) and (e) exhibit the graphical representations of the lattice. The equal-sized red circles in (a) indicate that excess material is on downward facing surfaces.

Table 4
Parameters for modeling a 3 x 3 x 3 I network lattice with 4 mm unit cell size and 0.292 volume fraction using the modeling procedure explained in Section 2.2.

C_1	C_2	C_3/mm	C_4/mm	C_5/mm	C_6	r
0.1	150	0	−0.5	0.18	3	−1.7418

discussed. In order to identify the required number of elements for TPMS lattices, a mesh convergence study on the CT-reconstructed lattice was performed in advance. In Fig. 8, technical stress–strain curves for different mesh resolutions are presented for a uniaxial compression test. Even though the stiffness and plateau stress decrease with increasing number of elements, the overall mesh influence proves to be marginal. The exponential increase after the horizontal course of the curve is caused by the onset of block compression. With the 196 k node model the convergence criterion is achieved, corresponding to a target element size of 0.3 mm and a minimum feature size of 0.05 mm for the 12 mm large lattices. The performance of ten node tetrahedral elements is found to be overall suitable for simulations of lattice structures, which is consistent with the findings of [23,71,72].

In figure Fig. 9, the technical stress–strain curves of the experiment and the simulation are plotted, whereas in Table 5, the corresponding characteristic values are listed. The latter include the compressive stiffness E, the compressive yield stress $\sigma_{c0.2}$, and the compressive stress at 26% compressive strain σ_{c26}, which is

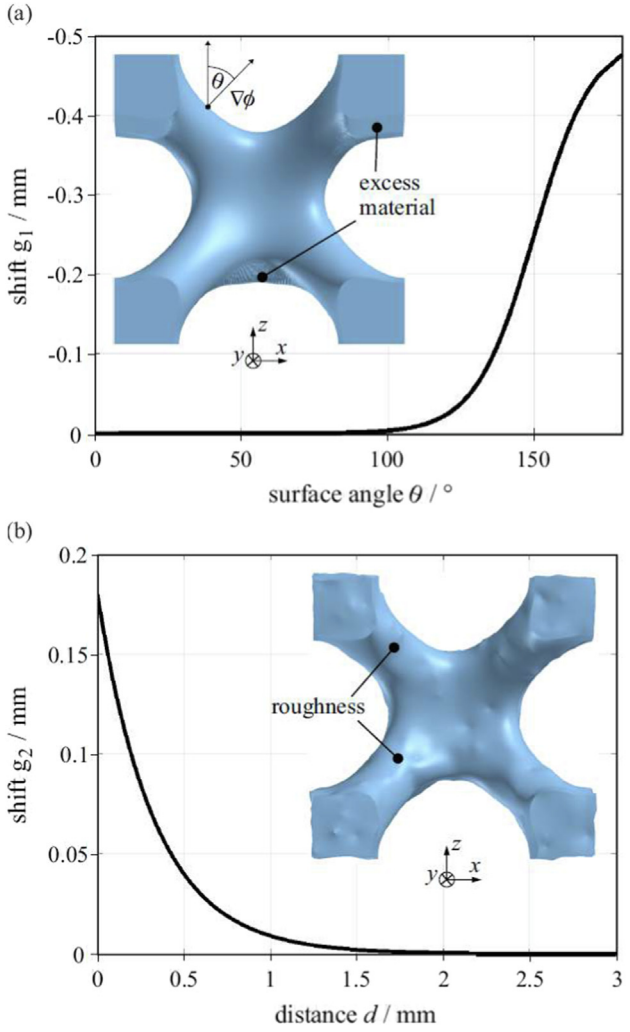

Fig. 6. According to Table 4 parameterized function 2 to model excess material on downward facing surfaces in (a), and function 3 to model surface roughness in (b). One sample unit cell with 4 mm edge length is shown for both modeling steps. The modeling details can be obtained from Section 2.2.

the maximum in the experiment. The simulation comprises the as-designed lattice, the as-built lattice, and the reconstructed lattice. Furthermore, the relative deviation from experiment to each of the numerical models $\Delta_{\text{rel.}}$ is given. It is worth mentioning that the experimental results are not statistically validated due to the limited specimen size. Nevertheless, it can be assumed that a general insight into of the actual mechanical behavior can be obtained, even if the mean value of a larger sample size should deviate.

For all lattices, the compressive stress–strain response shows similar characteristics to the bulk specimens: after the onset of plastic flow, an almost horizontal curve is obtained, with an even flatter slope than in the bulk specimens. Focusing first on the experimental results, it can be stated that both stiffness of about 1.6 GPa and compressive yield strength around 50 MPa are in the range of trabecular bone tissue [63,91]. For BTE, these properties are essential for preventing the stress-shielding effect and for ensuring structural integrity. The high elongation at failure of approximately 26% technical compressive strain is also advantageous for implants, as the risk of spontaneous failure can be counteracted. Although the dimensions of the lattice are probably too large for actual application, it is expected that rescaling would tend to improve the mechanical properties [84].

The strain distribution for $\bar{\varepsilon} = -0.26$ applied strain can be examined in more detail by referring to the DIC calculation in Fig. 10: the lattice exhibits a heterogeneous vertical strain distribution with significant concentrations in the struts. Here, the nodes of the lattice show more moderate values for the vertical strain in the interval $[-0.15, 0]$ compared to the struts with $[-0.6, -0.2]$. However, to what extent the DIC analysis evaluates the deformation for the deformed surface correctly remains uncertain. In particular, the combination of low volume fraction of the specimen and large deformation with failure progress is known to be challenging for optical measurements, cf. [92,93]. Therefore, the quantitative data should be treated with caution and it is assumed that locally larger actual strains tend to occur. In addition, a better equipped optical measurement setup would be useful in the future to enable spatial DIC analysis.

Nevertheless, the given DIC analysis in Fig. 10 provides insights into the deformation process of the lattice: the strain varies primarily between the different layers, but remains approximately equal within each layer. In the considered case, the strain increases from the top to the bottom layer of the lattice. At the end, a layer-by-layer collapse occurs. Since the test was stopped at the first collapse, failure occurred solely in the bottom layer. Anyway, it is expected that with further applied compressive strain, the other layers would gradually fail [83,94,36,64]. The heterogeneous strain distribution contradicts the uniform lattice design. The inconsistency is an indication of local imperfections that occur due to the manufacturing process. These must be addressed in the simulations, since they have a decisive influence on the mechanical behavior.

The numerical results of the as-designed lattice in Table 5 and Fig. 9 reveal significant differences compared to the experiment. As predicted from the morphological investigation in Section 3.2, the ideal design is accompanied by an overestimation of compressive stiffness (about 71%) as well as strengths (about 20% for $\sigma_{c0.2}$ and 12% for σ_{c26}). Consequently, the as-designed lattice is of limited informative value for the actual mechanics of the AM processed lattice.

In contrast, much better agreement is observed for the as-built model deduced immediately from CT data. Although stiffness is still overestimated by about 9%, the strength values are comparatively close to the experimental values. This outcome correlates with the literature [70,71] and was expected, since in the as-built lattice external imperfections are included. The slight discrepancy can be explained, firstly, by approximations during mesh generation and, secondly, by internal imperfections that were neglected in the simulation. Thirdly, the material model is subject to uncertainty, since only uniaxial tests on bulk specimens served for parameterization. In particular, not only the process parameters for the lattice differ slightly from those of the bulk specimens, but also the solidification conditions in the LPBF process due to the different specimen dimensions. Insights into the different microstructural states could be gained in the future by means of crystallographic and mechanical characterizations.

The best match is achieved with the reconstructed lattice: for the considered strain range, the numerical results match precisely with the experimental results. The percentage deviations are approximately -5% for the stiffness E and less than 1% for the strengths $\sigma_{c0.2}$ and σ_{c26}, cf. $\Delta_{\text{rel.}}$ in Table 5. It should be noted that the Boolean difference volume to the as-built lattice is about 4.93% for the reconstructed lattice. Nevertheless, this deviation is primarily due to the smaller scale morphological features such as roughness, which has a minor influence on the quasi-static mechanical behavior. More crucial is that the larger scale features associated with excess material are included.

Besides the good agreement between experiment and simulation for the single reconstructed lattice, the numerical result

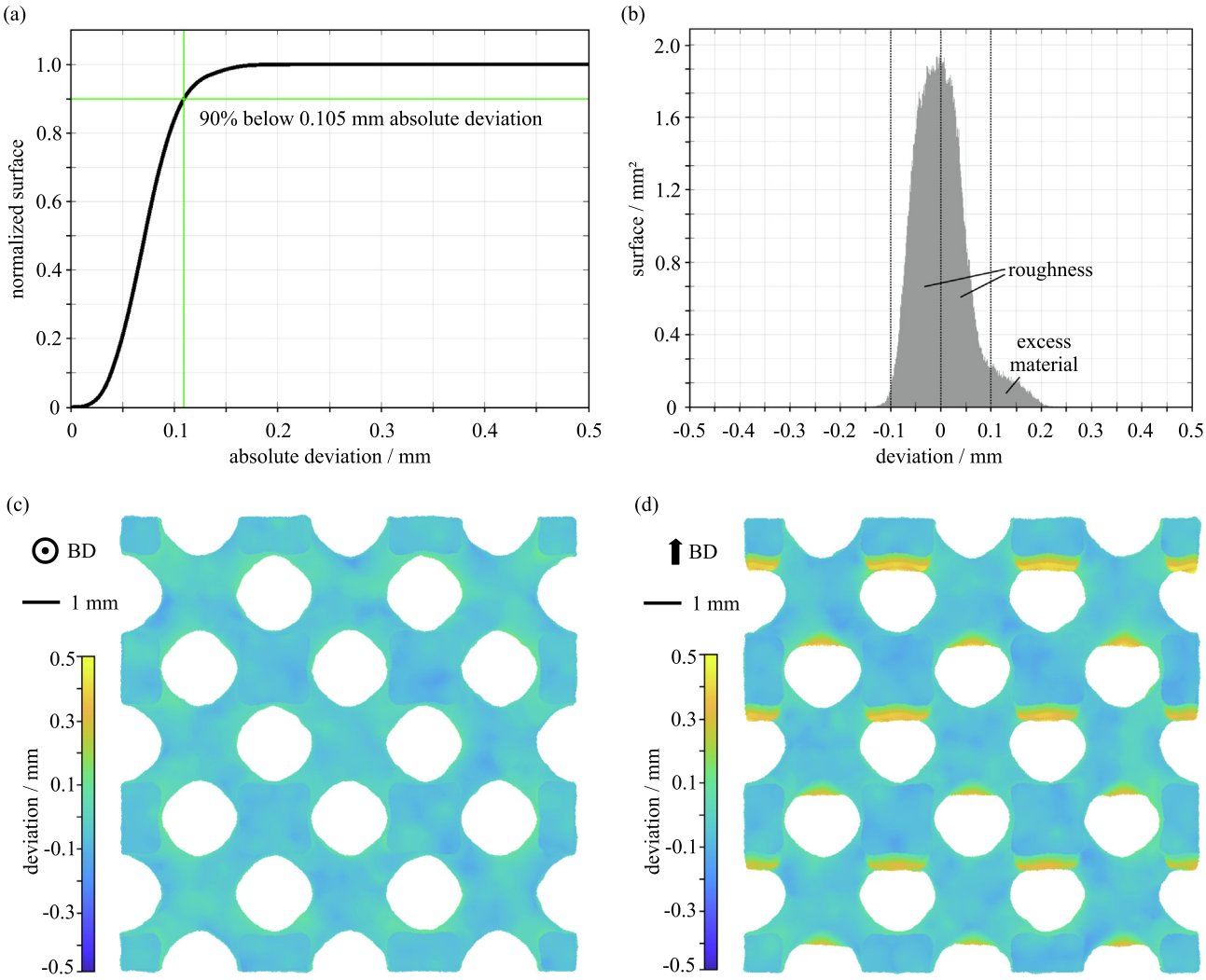

Fig. 7. Details for the morphological mismatch to the ideal lattice introduced by the modeling: (a) and (b) contain statistics, (c) and (d) show graphical representations for different views.

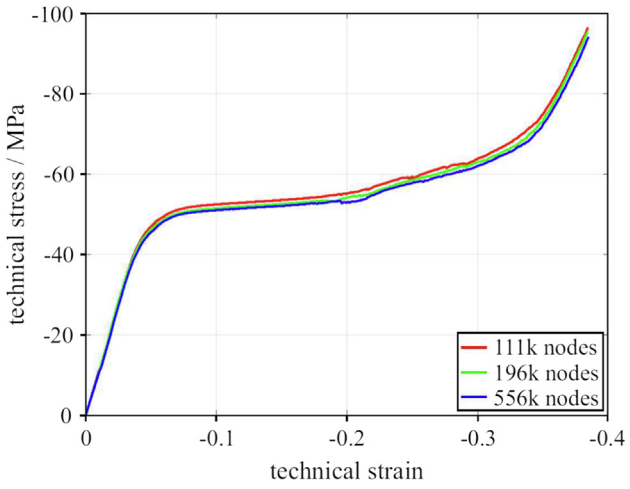

Fig. 8. Numerical stress–strain curves of different resolutions as-built I network lattice subjected to uniaxial compression test.

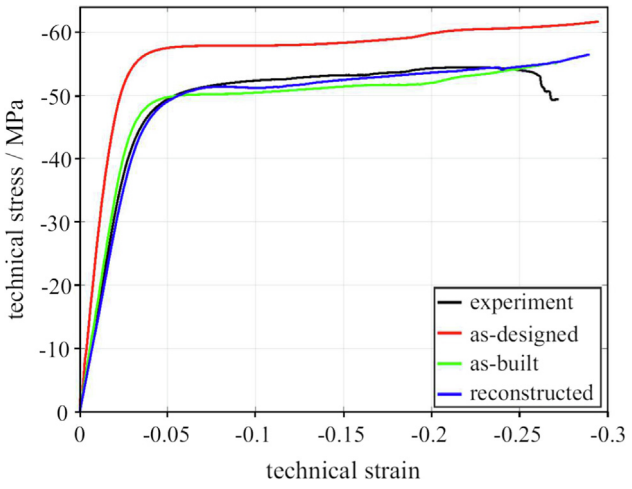

Fig. 9. Technical stress–strain curves from uniaxial compression tests on the I network lattice obtained by experiment and simulations.

Table 5
Mechanical properties for the I network lattice from uniaxial compression tests using experiment and simulation: E denotes the compressive stiffness, $\sigma_{c0.2}$ the compressive yield stress, σ_{c26} the compressive stress at −0.26 strain, and $\Delta_{rel.}$ denotes the relative deviation from the experiment to the three numerical models.

	E / GPa	$\sigma_{c0.2}$ / MPa	σ_{c26} / MPa	$\Delta_{rel.}(E)$	$\Delta_{rel.}(\sigma_{c0.2})$	$\Delta_{rel.}(\sigma_{c26})$
experiment	1.5685	42.124	54.701	-	-	-
as-designed	2.6888	50.65	61.141	0.7142	0.2024	0.1177
as-built	1.7117	44.673	55.04	0.0913	0.0605	0.0062
reconstructed	1.4894	42.029	55.037	−0.0504	−0.0023	0.0061

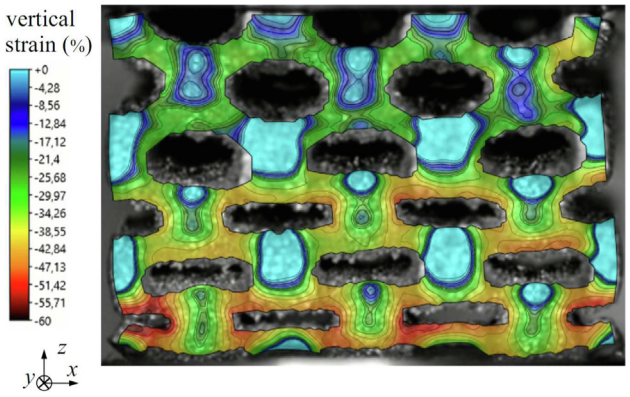

Fig. 10. DIC analysis of the vertical strain distribution at $\bar{\varepsilon} = -0.26$ technical strain in uniaxial compression test.

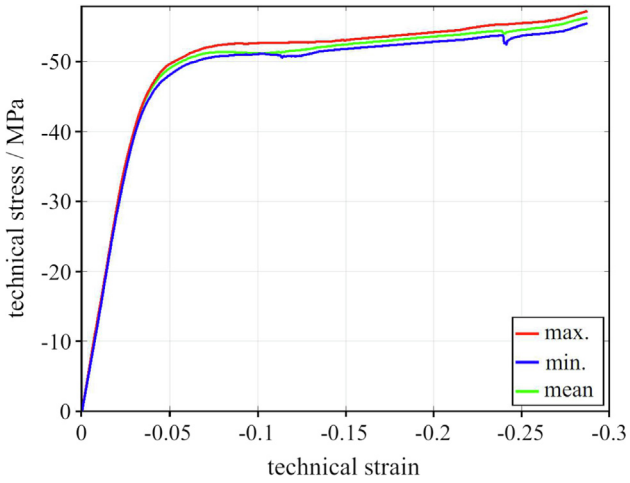

Fig. 11. Reproducibility study: shown are the interval and mean value of the technical stress–strain curve obtained with ten reconstructed I network lattices in uniaxial compression test.

proves to be reproducible. In Fig. 11, both the interval and the mean of the technical stress–strain curves from uniaxial compression test on ten reconstructed lattices can be found. The average absolute deviation (AAD) amounts to 0.4471 MPa, which corresponds to 0.793% in relative terms. This variation is comparatively small, so that reproducibility is given for the considered case. In this context, it should be emphasized that the statistical uncertainty of the semi-random modeling procedure is reflected one-to-one in the structure–property relationship. Thus, manufacturing-related imponderables that lead to non-unique structural behavior can be numerically taken into account. The amount of variation can be adjusted by the parameters C_5 and C_6 of the random surface roughness, cf. function 3.

In general, the interaction of the anisotropic elastoplastic model and the tension-pressure-dependent failure model is the pivotal factor for the proper evaluation of multiaxial stress states in lattices. The implemented material model proves to cover these aspects predominantly: both in the elastic and plastic regime, the model provides accurate results. Only the final phase involves inconsistency, as no damage or failure occurs in the simulation, in contrast to the experiment. This observation confirms the prediction from Section 3.2 that the modeling of failure is probably insufficient. To address this deficiency, future work should apply specimen geometries and loading scenarios in material characterization where stress states comparable to the lattice occur.

Finally, some general remarks on the investigation of the structural-property relationships should be highlighted:

- The key factor for the as-built/as-designed mismatch of the I network lattice is the excess material on downward facing surfaces. This leads to a more uneven material distribution among the nodes and struts in as-built models than in idealized as-design models. Since the excess material has only a subordinate load-bearing effect in the compression test, its presence effectively weakens the as-built morphology in experiment and simulation. The reconstructed model takes this fact into account and, therefore, provides decisively improved numerical results compared to the as-designed model. In particular, the measured compressive behavior prior to failure can be precisely replicated.
- The numerical results indicate that the volume fraction of a lattice is a limited descriptor for the structure–property relationships: even if the volume fraction is 0.292 in all simulations, the compressive behavior changes. In contrast, the Boolean difference volume to the as-built lattice emerges as a more suitable indicator, since here the morphology of the lattice is explicitly considered.
- Transferring the properties of the base material to lattice structures proves to be a reasonable approximation. Therefore, the calibration of the material parameters from Table 3 is comparatively straightforward. However, it should be noted that the specimen geometry actually affects the material properties: due to the large surface and the associated large temperature gradients in the LPBF process, the microstructure will develop differently in a lattice than in a bulk specimen. For this reason, the simulation results in this section are subject to uncertainties that may prove to be more decisive in other structural-property investigations.
- The formulation of the contact constraint between lattice and plate demands to be reviewed by sensitivity analyses, since considerable effects on the numerical results can ensue, cf. [72].
- The performed simulations do not consider internal imperfections such as pores, since only the external lattice shape was mimed. Although the present study indicated that quasi-static structural integrity is virtually independent of microporosity effects, this could be a critical shortcoming for other concerns. The literature review suggests that pores, for example, can significantly influence fatigue behavior [25,26,30,31,69,70]. Nevertheless, it can be assumed that due to the comparatively moderate thermal conductivity and reflectivity, internal porosity is not really a critical problem for Ti-42Nb alloys [95].

- In principle, the reconstruction procedure presented in Section 2.2 can be extended by adding further modeling functions g_i. In this way, previously neglected defect types can also be addressed. However, it is questionable to what extent this applies to internal imperfections: primarily, the proposed method is intended to mimic the external as-built morphology. Therefore, a coupled multiscale approach might be required for internal imperfections.

The overall promising findings for the proposed modeling procedure prompt the question of extensibility. This is investigated in the following section by applying the method to three additional TPMS network lattices.

3.4. Extension to further TPMS lattices

In this section, the extensibility of the modeling procedure from Section 2.2 is investigated. If proven feasible, this would be the first step in becoming less dependent on limited available CT data in the future. Indeed, once the modeling parameters from Table 4 are determined for specific TPMS lattices and process parameters, the as-built morphology can be reconstructed in a simplified manner. In this way, valuable insights into the actual performance could be gained nondestructively and without high-quality instrumentation. In particular, three further 3x3x3 TPMS network lattices with the same volume fraction, size and material as the studied I network lattice are considered. These lattices are based on Schwarz Primitive (P), Schoen Gyroid (G) and Schwarz Diamond (D) network TPMS.

The modeling procedure is the same as for the I network lattice detailed in Section 2.1 and 2.2, and the corresponding level set functions are available in the literature, e.g. [3,13,64]. For the new lattices, both the modeling parameters for reconstructing from Table 4 and the parameters of the material model from Table 3 are adopted from the I network lattice. In Fig. 12(a), the morphology of the as-designed and the reconstructed model are respectively contrasted. Without a comprehensive analysis of the reconstructed models, two main findings can be drawn: firstly, the modeling procedure can be transferred to the further investigated TPMS lattices. This is probably true for any TPMS lattice, either in network or sheet configuration. However, to what extent the numerically reconstructed lattices match the as-built ones remains, of course, uncertain. Secondly, according to the different lattice shapes in connection with the modeling procedure, the primary morphological mismatch is differently distributed and occurs to different extents. In order to quantify this more precisely, the critical surface fraction $A_{\text{crit.}}$, i.e. the surface fraction with more than 45° overhang, is determined for the individual lattices.

In Figure Fig. 12(b), the obtained values for P, D, G, and I network lattices are compared depending on the volume fraction. It is found that the critical surface fractions for the four lattices differ significantly: independent of the volume fraction, P network lattice exhibits the lowest critical surface fraction for the considered lattices, whereas I network lattice shows the highest values. The fractions of D and G network lattices are almost identical and are located in between. Since the extent of the citical overhang decisively affects the manufacturability by LPBF, it can be assumed that the difference for the TPMS lattices is expressed in different manufacturability and quality of the processed structures. In particular, it can be expected that I network lattices are more challenging to fabricate compared especially with P network lattices, but also with D and G lattices. This hypothesis is partially confirmed by the results reported in [13], where the manufacturability of different TPMS lattices is investigated. As shown there, I network lattices tend to increased morphological mismatch in the range of $0.25 - 0.5$ volume fraction compared to D and G network lattices.

To investigate the morphology dependence of the modeling procedure, uniaxial compression tests are simulated according to Fig. 3(c) for P, D, G and I network lattices. The specified strain is reduced to -0.1 since the experimentally confirmed validity of the material model is limited to the initial strain range. In each case the as-designed as well as the reconstructed model are considered. Moreover, the reproducibility of the numerical results for the different TPMS types is investigated separately. Here, no particular correlation is detected and the scatter is similar to the I network lattice, cf. Fig. 11. Analogous to the I network lattice, the results are therefore predicated on a single model in each case. The corresponding technical stress–strain curves can be obtained from Fig. 12c) and the characteristic properties from Table 6.

The qualitative comparison of the stress–strain curves shows that different TPMS lattices differ in stiffness and strength. This can be attributed to the morphology in conjunction with the posed FE boundary value problem and agrees with the literature, e.g. [36,53,60,96]. In addition, a regular correlation between the results of as-designed and the reconstructed state can be observed for the individual TPMS types: in all cases both the stiffness and strength of the as-designed lattice exceeds those of the reconstructed one. This can be quantified by examining the compressive stiffness as well as the compressive stress at -10% technical axial strain σ_{c10} in Table 6: the stiffness of the reconstructed model is reduced by about $30\% - 42\%$ compared to the as-designed model and for the strength the reduction is about $2.2\% - 11.5\%$. Comparison of the as-designed and reconstructed lattice in Fig. 12(a) yields potential causes for the finding: similar to the I network lattice in Section 2.2, besides the random shaped surface associated with roughness, excess material is systematically generated at downward facing surfaces. This non-load bearing accumulation of material presumably leads to mechanical softening since the overall amount of material remains constant. So again, redistribution of material is the primary driver of the weakened morphology.

Closer inspection reveals that the larger the critical surface fraction, the larger the mechanical impairment, cf. Table 6 and Fig. 12(-b)-(c). In particular, the characteristic properties of the P network lattice decrease relatively less than those of the other TPMS types: in stiffness, about 30% compared to $33\% - 42\%$, and in strength, about 2.2% compared to $3\% - 11.5\%$. Thereby, the critical surface fraction of the P network lattice amounts 6.1%, which is much less than for the other lattices with $11.4\% - 15.4\%$. Conversely, the decrease is maximal for the I network lattice, which possesses the largest critical surface fraction. This one-to-one correlation is remarkable, since numerically a measurable relationship between structural property and structural integrity is established. So far, additive manufacturability is commonly evaluated qualitatively and based on experience, cf. [13,27,30,68]. Should the finding be confirmed experimentally, a priori statements could be derived in the future about the expected manufacturability and the associated actual structural behavior. Moreover, it is worth mentioning that the morphological modification is generally accompanied by a reduction in stiffness and strength compared to the as-designed lattice. For this reason, design procedures based on reconstructed models are more conservative and reliable than those based on as-designed models.

Concluding, the proposed modeling procedure can potentially be applied to any material and TPMS type. Given the material data and the CT scan, both the as-built morphology and the structure–property relationship can be approximately reconstructed. In particular, the material characterizations already published in the literature for many AM-relevant materials can be accessed. In addition, it should be emphasized that CT data are often not available, especially in practice, due to the component dimensions and the required effort. Then appropriate conservative estimates are necessary. To this end, the presented method offers a proposal as

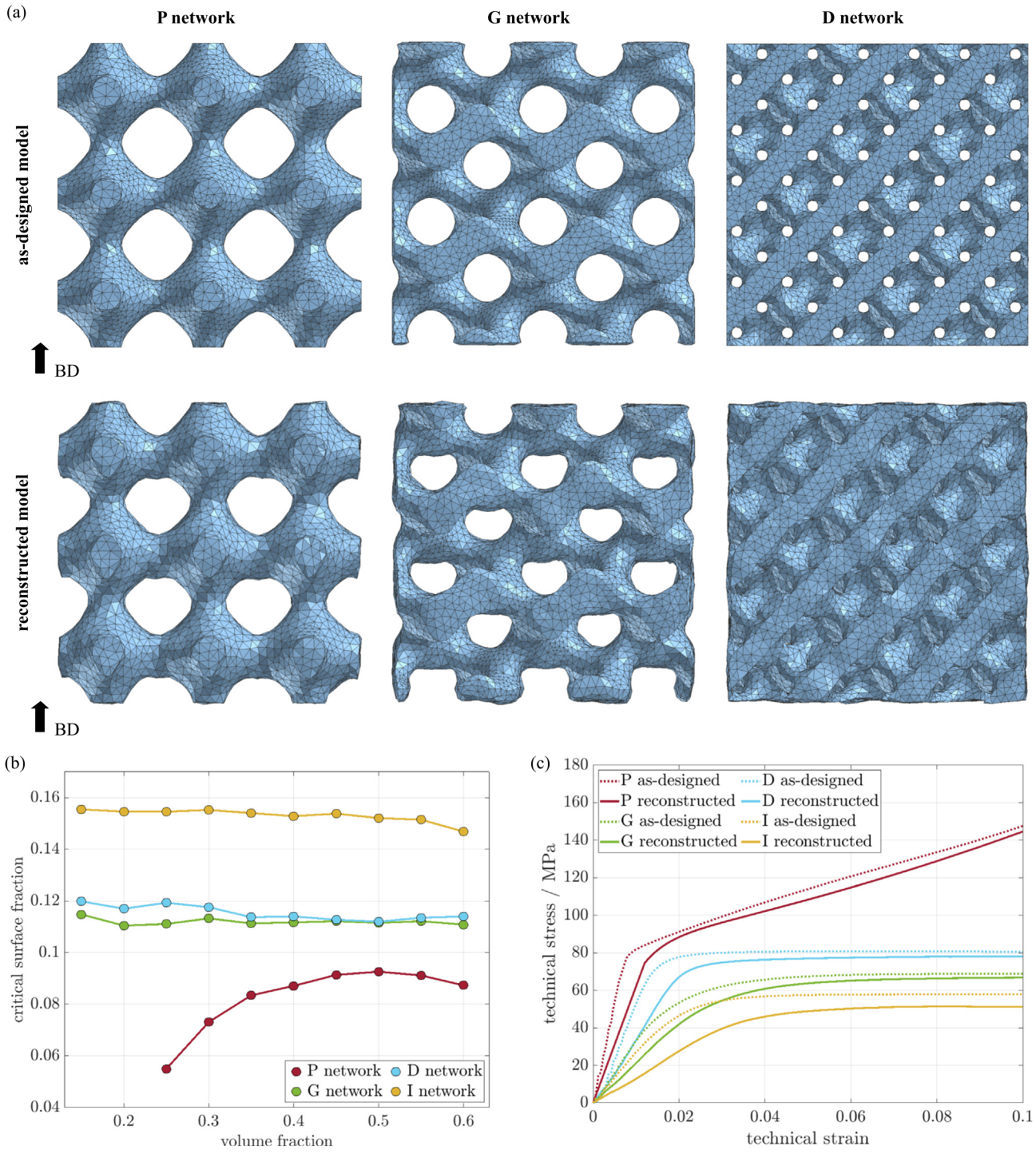

Fig. 12. Overview of extended numerical work for additional TPMS network lattices with 3 x 3 x 3 unit cells of 4 mm size and 0.27 volume fraction: in (a), the as-designed and the reconstructed morphology of P, D and G network lattices are respectively contrasted, in (b), the critical surface fraction (i.e., the surface fraction with more than 45° overhang) is plotted over the volume fraction, and in (c), the technical stress–strain curves for uniaxial compression tests are shown.

Table 6
Numerical results for different TPMS network lattices with 0.27 volume fraction obtained by compression tests, each for the as-designed and reconstructed model. Here, E denotes the compressive stiffness, σ_{c10} denotes the compressive stress at −10% technical axial strain, $A_{crit.}$ denotes the critical surface fraction at 0.27 volume fraction, and $\Delta_{rel.}$ denotes the relative change from the as-designed to the reconstructed model, either from E or σ_{c10}.

TPMS	model	E / GPa	σ_{c10} / MPa	$A_{crit.}$	$\Delta_{rel.}(E)$	$\Delta_{rel.}(\sigma_{c10})$
P network	as-designed	10.231	147.75	0.0611	−0.3009	−0.0218
	reconstructed	7.1529	144.53			
G network	as-designed	3.2592	68.851	0.1138	−0.3515	−0.0296
	reconstructed	2.1136	66.812			
D network	as-designed	5.1954	80.485	0.1189	−0.3283	−0.0309
	reconstructed	3.4898	77.996			
I network	as-designed	2.5785	57.8625	0.1541	−0.4224	−0.1154
	reconstructed	1.4894	51.186			

the morphological mismatch is inserted independently instead of relying on one-to-one adaptation from CT scans. In particular, the distinctive AM mesostructure is mimicked, but not copied. The loss of accuracy is countered by the extensibility, since informed predictions for any TPMS lattice can be achieved. Nevertheless, to what extent the numerical results reflect reality remains uncertain without experimental studies. However, at least in the case of the I network lattice, the modeling procedure accurately reproduces the real conditions, cf. Fig. 9 and Table 5.

4. Conclusion

The promising potential of TPMS lattices can only be technically exploited if their structural integrity is ensured. A basic prerequisite for this is the consideration of process-related imperfections already during design. However, suitable modeling concepts and dimensioning guidelines have been lacking in literature so far.

Therefore, in this study, the structure–property relationships of additively manufactured TPMS lattices were examined experimentally and numerically. In particular, the Schoen I-WP network lattice made of LPBF processed Ti-42Nb with 3x3x3 unit cells, a volume fraction of 0.27, and a unit cell size of 4mm was investigated. The main focus was on the numerical reconstruction of the as-built morphology containing external imperfections such as surface roughness and excess material on downward facing surfaces. For this purpose, a semi-random multi-step modeling procedure was introduced to redistribute the material of TPMS lattices according to CT data. The following conclusions can be drawn:

- LPBF processed biocompatible Ti-42Nb alloy emerges as promising candidate for implant applications due to the combination of low Young's modulus along with high strengths and elongations at failure.
- The implemented finite element material model incorporating orthotropic elasticity, Raghava-Hill plasticity and Johnson–Cook failure enables to capture the experimentally determined tensile and compressive behavior of bulk specimens.
- In I-WP network lattice fabricated by LPBF, besides randomly distributed surface roughness, regularly arranged excess material on downward facing surfaces occurs. This morphological mismatch significantly affects the mechanical performance, due to the resulting TPMS atypical strain localization during uniaxial compression tests.
- The as-built morphology of I-WP network lattice can be numerically reconstructed by selective modification of the ideal design. Here, the Boolean difference volume with respect to the as-built lattice derived from CT data proves to be a convenient descriptor for evaluating reconstruction.
- The reconstructed models enable an accurate simulation of the experimentally observed structure–property relationships. This particularly applies to the compressive behavior, where the strengths have been calculated with relative deviations below 1%. Such high prediction accuracy is a prerequisite for future clinical use in BTE.
- In terms of critical surface overhang, TPMS network lattices based on the Schwarz Primitive surface are advantageous compared to the Schoen Gyroid and Schwarz Diamond surface for AM. In contrast, the Schoen I-WP network is the most challenging TPMS lattice type due to the large surface fraction with overhang exceeding 45°. Furthermore, a numerical correlation is observed between the critical surface fraction and the degradation of mechanical properties in terms of stiffness and strength.
- The modeling procedure proves to be applicable in principle to any TPMS based lattice and to any material. In this way, the mandatory dependence on high-quality instrumentation can be put into perspective once characteristic modeling parameters have been experimentally determined: at least for similar material-process-lattice combinations, informed and conservative predictions of the actual structural behavior can be obtained by one-to-one parameter transfer even without new CT data.

The overall convincing findings suggest to employ the presented methodology for further structure–property investigations. Therefore, future work will investigate the influence of different LPBF process parameters, cell types, and cell sizes on process-related imperfections and identify characteristic modeling parameters. In particular, the extent to which the defect types considered so far are already sufficient for the numerical reconstruction of different in other lattices will be addressed. Possibly other drivers of morphological mismatch are prevalent here, so that further modeling functions need to be introduced. Once representative modeling parameters have been calibrated by such a screening, predictions about the distinctive AM-related morphology of various TPMS lattices will be feasible in the future. In addition, the influence of AM-typical imperfections such as surface roughness and excess material on downward facing surfaces on the structure–property relationships will be analyzed individually. Here, the full potential of the proposed modeling procedure unfolds since different error types can be easily isolated, which is experimentally impossible. If the results and hypotheses stated in this paper are confirmed in the planned work, far-reaching implications would arise both for structure–property research and for practical handling.

Funding

Acknowledgement is made for the funding by the Deutsche Forschungsgemeinschaft (DFG) within the research projects ZI/1006/16–1 and GE/1106/12–1 (No. 419952351).

Declaration of Competing Interest

The authors declare that they have no known competing financial interests or personal relationships that could have appeared to influence the work reported in this paper.

Acknowledgements

The authors gratefully acknowledge the assistance of S. Schettler with the mechanical experiments. Furthermore, the support of T. Gustmann and U. Kühn with respect to fruitful scientific discussions is acknowledged.

References

[1] C.M. Murphy, M.G. Haugh, F.J. O'brien, The effect of mean pore size on cell attachment, proliferation and migration in collagen–glycosaminoglycan scaffolds for bone tissue engineering, Biomaterials 31 (3) (2010) 461–466. doi: 10.1016/j.biomaterials.2009.09.063.

[2] C. Torres-Sanchez, F. Al Mushref, M. Norrito, K. Yendall, Y. Liu, P. Conway, The effect of pore size and porosity on mechanical properties and biological response of porous titanium scaffolds, Mater. Sci. Eng.: C 77 (2017) 219–228, https://doi.org/10.1016/j.msec.2017.03.249. URL https://www.sciencedirect.com/science/article/pii/S092849311632793X.

[3] F. Günther, M. Wagner, S. Pilz, A. Gebert, M. Zimmermann, Design procedure for triply periodic minimal surface based biomimetic scaffolds, J. Mech. Behav. Biomed. Mater. 126 (2022) 104871, https://doi.org/10.1016/j.jmbbm.2021.104871.

[4] H. Otera, K. Mihara, Molecular mechanisms and physiologic functions of mitochondrial dynamics, J. Biochem. 149 (3) (2011) 241–251, https://doi.org/10.1093/jb/mvr002.

[5] A.R. Amini, C.T. Laurencin, S.P. Nukavarapu, Bone tissue engineering: recent advances and challenges, Critical Reviews™ in Biomedical Engineering 40 (5). doi: 10.1615/critrevbiomedeng.v40.i5.10.

[6] M.A. Khorshidi, Length scale parameter of single trabecula in cancellous bone, Biomech. Model. Mechanobiol. 19 (5) (2020) 1917–1923, https://doi.org/10.1007/s10237-020-01316-5.

[7] V. Kauschke, A. Gebert, M. Calin, J. Eckert, S. Scheich, C. Heiss, K.S. Lips, Effects of new beta-type ti-40nb implant materials, brain-derived neurotrophic factor, acetylcholine and nicotine on human mesenchymal stem cells of osteoporotic and non osteoporotic donors, PLoS One 13 (2) (2018) e0193468, https://doi.org/10.1371/journal.pone.0193468.

[8] S. Pilz, A. Gebert, A. Voss, S. Oswald, M. Göttlicher, U. Hempel, J. Eckert, M. Rohnke, J. Janek, M. Calin, Metal release and cell biological compatibility of beta-type ti-40nb containing indium, J. Biomed. Mater. Res. Part B: Appl. Biomater. 106 (5) (2018) 1686–1697, https://doi.org/10.1002/jbm.b.33976.

[9] G. Lewis, Properties of open-cell porous metals and alloys for orthopaedic applications, J. Mater. Sci.: Mater. Med. 24 (10) (2013) 2293–2325, https://doi.org/10.1007/s10856-013-4998-y.

[10] S. Arabnejad, R.B. Johnston, J.A. Pura, B. Singh, M. Tanzer, D. Pasini, High-strength porous biomaterials for bone replacement: A strategy to assess the interplay between cell morphology, mechanical properties, bone ingrowth and manufacturing constraints, Acta Biomater. 30 (2016) 345–356, https://doi.org/10.1016/j.actbio.2015.10.048.

[11] B. Charbonnier, M. Manassero, M. Bourguignon, A. Decambron, H. El-Hafci, C. Morin, D. Leon, M. Bensidoum, S. Corsia, H. Petite, et al., Custom-made macroporous bioceramic implants based on triply-periodic minimal surfaces for bone defects in load-bearing sites, Acta Biomater. 109 (2020) 254–266, https://doi.org/10.1016/j.actbio.2020.03.016.

[12] A. Di Luca, A. Longoni, G. Criscenti, C. Mota, C. van Blitterswijk, L. Moroni, Toward mimicking the bone structure: design of novel hierarchical scaffolds with a tailored radial porosity gradient, Biofabrication 8 (4) (2016) 045007, https://doi.org/10.1088/1758-5090/8/4/045007.

[13] D. Barba, E. Alabort, R. Reed, Synthetic bone: design by additive manufacturing, Acta Biomater. 97 (2019) 637–656, https://doi.org/10.1016/j.actbio.2019.07.049.

[14] F.M. Klenke, Y. Liu, H. Yuan, E.B. Hunziker, K.A. Siebenrock, W. Hofstetter, Impact of pore size on the vascularization and osseointegration of ceramic bone substitutes in vivo, Journal of Biomedical Materials Research Part A: An Official Journal of The Society for Biomaterials, The Japanese Society for Biomaterials, and The Australian Society for Biomaterials and the Korean Society for Biomaterials 85 (3) (2008) 777–786, https://doi.org/10.1002/jbm.a.31559.

[15] N. Taniguchi, S. Fujibayashi, M. Takemoto, K. Sasaki, B. Otsuki, T. Nakamura, T. Matsushita, T. Kokubo, S. Matsuda, Effect of pore size on bone ingrowth into porous titanium implants fabricated by additive manufacturing: an in vivo experiment, Materials Science and Engineering: C 59 (2016) 690–701, https://doi.org/10.1016/j.msec.2015.10.069.

[16] L. Gibson, Mechanical behavior of metallic foams, Annual review of materials science 30 (1) (2000) 191–227, https://doi.org/10.1146/annurev.matsci.30.1.191.

[17] A.A. Zadpoor, Bone tissue regeneration: the role of scaffold geometry, Biomaterials science 3 (2) (2015) 231–245, https://doi.org/10.1039/C4BM00291A.

[18] S.B. Blanquer, M. Werner, M. Hannula, S. Sharifi, G.P. Lajoinie, D. Eglin, J. Hyttinen, A.A. Poot, D.W. Grijpma, Surface curvature in triply-periodic minimal surface architectures as a distinct design parameter in preparing advanced tissue engineering scaffolds, Biofabrication 9 (2) (2017) 025001, https://doi.org/10.1088/1758-5090/aa6553.

[19] S.J. Callens, R.J. Uyttendaele, L.E. Fratila-Apachitei, A.A. Zadpoor, Substrate curvature as a cue to guide spatiotemporal cell and tissue organization, Biomaterials 232 (2020) 119739, https://doi.org/10.1016/j.biomaterials.2019.119739.

[20] L. Boniotti, S. Beretta, L. Patriarca, L. Rigoni, S. Foletti, Experimental and numerical investigation on compressive fatigue strength of lattice structures of alsi7mg manufactured by slm, Int. J. Fatigue 128 (2019) 105181, https://doi.org/10.1016/j.ijfatigue.2019.06.041.

[21] A.A. Zadpoor, Mechanical performance of additively manufactured meta-biomaterials, Acta Biomater. 85 (2019) 41–59, https://doi.org/10.1016/j.actbio.2018.12.038.

[22] D. Mahmoud, M. Elbestawi, Selective laser melting of porosity graded lattice structures for bone implants, The International Journal of Advanced Manufacturing Technology 100 (9) (2019) 2915–2927, https://doi.org/10.1007/s00170-018-2886-9.

[23] L. Liu, P. Kamm, F. García-Moreno, J. Banhart, D. Pasini, Elastic and failure response of imperfect three-dimensional metallic lattices: the role of geometric defects induced by selective laser melting, J. Mech. Phys. Solids 107 (2017) 160–184, https://doi.org/10.1016/j.jmps.2017.07.003.

[24] R. Wauthle, B. Vrancken, B. Beynaerts, K. Jorissen, J. Schrooten, J.-P. Kruth, J. Van Humbeeck, Effects of build orientation and heat treatment on the microstructure and mechanical properties of selective laser melted ti6al4v lattice structures, Additive Manufacturing 5 (2015) 77–84, https://doi.org/10.1016/j.addma.2014.12.008.

[25] A. Du Plessis, S.M.J. Razavi, F. Berto, The effects of microporosity in struts of gyroid lattice structures produced by laser powder bed fusion, Mater. Des. 194 (2020) 108899, https://doi.org/10.1016/j.matdes.2020.108899.

[26] K. Lietaert, A. Cutolo, D. Boey, B. Van Hooreweder, Fatigue life of additively manufactured ti6al4v scaffolds under tension-tension, tension-compression and compression-compression fatigue load, Scientific reports 8 (1) (2018) 1–9, https://doi.org/10.1038/s41598-018-23414-2.

[27] O. Al-Ketan, M. Pelanconi, A. Ortona, R.K. Abu Al-Rub, Additive manufacturing of architected catalytic ceramic substrates based on triply periodic minimal surfaces, Journal of the American Ceramic Society 102 (10) (2019) 6176–6193. doi: 10.1111/jace.16474.

[28] S. Liu, Y.C. Shin, Additive manufacturing of ti6al4v alloy: A review, Mater. Des. 164 (2019) 107552, https://doi.org/10.1016/j.matdes.2018.107552.

[29] P. Li, D. Warner, A. Fatemi, N. Phan, Critical assessment of the fatigue performance of additively manufactured ti–6al–4v and perspective for future research, Int. J. Fatigue 85 (2016) 130–143, https://doi.org/10.1016/j.ijfatigue.2015.12.003.

[30] M. Benedetti, A. Du Plessis, R. Ritchie, M. Dallago, S. Razavi, F. Berto, Architected cellular materials: A review on their mechanical properties towards fatigue-tolerant design and fabrication, Materials Science and Engineering: R: Reports 144 (2021) 100606, https://doi.org/10.1016/j.mser.2021.100606.

[31] I. Echeta, X. Feng, B. Dutton, R. Leach, S. Piano, Review of defects in lattice structures manufactured by powder bed fusion, The International Journal of Advanced Manufacturing Technology 106 (5) (2020) 2649–2668, https://doi.org/10.1007/s00170-019-04753-4.

[32] D.-J. Yoo, Computer-aided porous scaffold design for tissue engineering using triply periodic minimal surfaces, International Journal of Precision Engineering and Manufacturing 12 (1) (2011) 61–71, https://doi.org/10.1007/s12541-011-0008-9.

[33] X.-Y. Zhang, G. Fang, L.-L. Xing, W. Liu, J. Zhou, Effect of porosity variation strategy on the performance of functionally graded ti-6al-4v scaffolds for bone tissue engineering, Mater. Des. 157 (2018) 523–538, https://doi.org/10.1016/j.matdes.2018.07.064.

[34] M. Zhianmanesh, M. Varmazyar, H. Montazerian, Fluid permeability of graded porosity scaffolds architectured with minimal surfaces, ACS Biomaterials Science & Engineering 5 (3) (2019) 1228–1237, https://doi.org/10.1021/acsbiomaterials.8b01400.

[35] L. Li, J. Shi, K. Zhang, L. Yang, F. Yu, L. Zhu, H. Liang, X. Wang, Q. Jiang, Early osteointegration evaluation of porous ti6al4v scaffolds designed based on triply periodic minimal surface models, Journal of Orthopaedic, Translation 19 (2019) 94–105, https://doi.org/10.1016/j.jot.2019.03.003.

[36] O. Al-Ketan, R. Rowshan, R.K.A. Al-Rub, Topology-mechanical property relationship of 3d printed strut, skeletal, and sheet based periodic metallic cellular materials, Additive Manufacturing 19 (2018) 167–183, https://doi.org/10.1016/j.addma.2017.12.006.

[37] C. Yan, L. Hao, A. Hussein, S.L. Bubb, P. Young, D. Raymont, Evaluation of light-weight alsi10mg periodic cellular lattice structures fabricated via direct metal laser sintering, J. Mater. Process. Technol. 214 (4) (2014) 856–864, https://doi.org/10.1016/j.jmatprotec.2013.12.004.

[38] S. Torquato, A. Donev, Minimal surfaces and multifunctionality, Proceedings of the Royal Society of London. Series A: Mathematical, Physical and Engineering Sciences 460 (2047) (2004) 1849–1856. doi: 10.1098/rspa.2003.1269.

[39] Acoustic band gaps and elastic stiffness of pmma cellular solids based on triply periodic minimal surfaces, Mater. Des. 145 (2018) 20–27. doi:https://doi.org/10.1016/j.matdes.2018.02.032.
[40] E. Liverani, A.H. Lutey, A. Fortunato, A. Ascari, Characterization of lattice structures for additive manufacturing of lightweight mechanical components, in: International Manufacturing Science and Engineering Conference, Vol. 50732, American Society of Mechanical Engineers, 2017, p. V002T01A012. doi: 10.1115/MSEC2017-2835.
[41] N. Thomas, N. Sreedhar, O. Al-Ketan, R. Rowshan, R.K.A. Al-Rub, H. Arafat, 3d printed spacers based on tpms architectures for scaling control in membrane distillation, J. Membr. Sci. 581 (2019) 38–49, https://doi.org/10.1016/j.memsci.2019.03.039.
[42] M.D. Turner, M. Saba, Q. Zhang, B.P. Cumming, G.E. Schröder-Turk, M. Gu, Miniature chiral beamsplitter based on gyroid photonic crystals, Nat. Photonics 7 (10) (2013) 801–805.
[43] H. Peng, F. Gao, W. Hu, Design, modeling and characterization of triply periodic minimal surface heat exchangers with additive manufacturing, in: 30th Annual International Solid Freeform Fabrication Symposium–An Additive Manufacturing Conference, 2019.
[44] J. Kim, D.-J. Yoo, 3d printed compact heat exchangers with mathematically defined core structures, Journal of Computational Design and Engineering 7 (4) (2020) 527–550.
[45] S. Vijayavenkataraman, L. Zhang, S. Zhang, J.Y. Hsi Fuh, W.F. Lu, Triply periodic minimal surfaces sheet scaffolds for tissue engineering applications: An optimization approach toward biomimetic scaffold design, ACS Applied Bio Materials 1 (2) (2018) 259–269. doi: 10.1021/acsabm.8b00052.
[46] J.M. Walker, E. Bodamer, A. Kleinfehn, Y. Luo, M. Becker, D. Dean, Design and mechanical characterization of solid and highly porous 3d printed poly (propylene fumarate) scaffolds, Progress in Additive Manufacturing 2 (1) (2017) 99–108, https://doi.org/10.1007/s40964-017-0021-3.
[47] Y. Wang, X. Ren, Z. Chen, Y. Jiang, X. Cao, S. Fang, T. Zhao, Y. Li, D. Fang, Numerical and experimental studies on compressive behavior of gyroid lattice cylindrical shells, Mater. Des. 186 (2020) 108340, https://doi.org/10.1016/j.matdes.2019.108340.
[48] Additive manufacturing and mechanical characterization of graded porosity scaffolds designed based on triply periodic minimal surface architectures, Journal of the Mechanical Behavior of Biomedical Materials 62 (2016) 481–494. doi:https://doi.org/10.1016/j.jmbbm.2016.05.027.
[49] M. Afshar, A. Pourkamali Anaraki, H. Montazerian, Compressive characteristics of radially graded porosity scaffolds architectured with minimal surfaces, Materials Science and Engineering: C 92 (2018) 254–267, https://doi.org/10.1016/j.msec.2018.06.051.
[50] S. Yu, J. Sun, J. Bai, Investigation of functionally graded tpms structures fabricated by additive manufacturing, Mater. Des. 182 (2019) 108021, https://doi.org/10.1016/j.matdes.2019.108021.
[51] S.-D. Yang, H.G. Lee, J. Kim, A phase-field approach for minimizing the area of triply periodic surfaces with volume constraint, Comput. Phys. Commun. 181 (6) (2010) 1037–1046, https://doi.org/10.1016/j.cpc.2010.02.010.
[52] D.-J. Yoo, Advanced porous scaffold design using multi-void triply periodic minimal surface models with high surface area to volume ratios, International journal of precision engineering and manufacturing 15 (8) (2014) 1657–1666, https://doi.org/10.1007/s12541-014-0516-5.
[53] S.C. Kapfer, S.T. Hyde, K. Mecke, C.H. Arns, G.E. Schröder-Turk, Minimal surface scaffold designs for tissue engineering, Biomaterials 32 (29) (2011) 6875–6882, https://doi.org/10.1016/j.biomaterials.2011.06.012.
[54] A. Castro, T. Pires, J. Santos, B. Gouveia, P. Fernandes, Permeability versus design in tpms scaffolds, Materials 12 (8) (2019) 1313, https://doi.org/10.3390/ma12081313.
[55] S. Ma, Q. Tang, X. Han, Q. Feng, J. Song, R. Setchi, Y. Liu, Y. Liu, A. Goulas, D.S. Engstrøm, et al., Manufacturability, mechanical properties, mass-transport properties and biocompatibility of triply periodic minimal surface (tpms) porous scaffolds fabricated by selective laser melting, Mater. Des. 195 (2020) 109034, https://doi.org/10.1016/j.matdes.2020.109034.
[56] G. Yu, Z. Li, S. Li, Q. Zhang, Y. Hua, H. Liu, X. Zhao, D.T. Dhaidhai, W. Li, X. Wang, The select of internal architecture for porous ti alloy scaffold: a compromise between mechanical properties and permeability, Mater. Des. 192 (2020) 108754.
[57] H. Montazerian, E. Davoodi, M. Asadi-Eydivand, J. Kadkhodapour, M. Solati-Hashjin, Porous scaffold internal architecture design based on minimal surfaces: A compromise between permeability and elastic properties, Mater. Des. 126 (2017) 98–114, https://doi.org/10.3390/sym10090361.
[58] L. Yang, C. Yan, C. Han, P. Chen, S. Yang, Y. Shi, Mechanical response of a triply periodic minimal surface cellular structures manufactured by selective laser melting, Int. J. Mech. Sci. 148 (2018) 149–157, https://doi.org/10.1016/j.ijmecsci.2018.08.039.
[59] R. Asbai-Ghoudan, S.R. de Galarreta, N. Rodriguez-Florez, Analytical model for the prediction of permeability of triply periodic minimal surfaces, J. Mech. Behav. Biomed. Mater. (2021) 104804, https://doi.org/10.1016/j.jmbbm.2021.104804.
[60] H. Montazerian, M. Mohamed, M.M. Montazeri, S. Kheiri, A. Milani, K. Kim, M. Hoorfar, Permeability and mechanical properties of gradient porous pdms scaffolds fabricated by 3d-printed sacrificial templates designed with minimal surfaces, Acta Biomater. 96 (2019) 149–160, https://doi.org/10.1016/j.actbio.2019.06.040.
[61] H.A. Zaharin, A.M. Abdul Rani, F.I. Azam, T.L. Ginta, N. Sallih, A. Ahmad, N.A. Yunus, T.Z.A. Zulkifli, Effect of unit cell type and pore size on porosity and mechanical behavior of additively manufactured ti6al4v scaffolds, Materials 11 (12) (2018) 2402, https://doi.org/10.3390/ma11122402.
[62] T. Maconachie, M. Leary, B. Lozanovski, X. Zhang, M. Qian, O. Faruque, M. Brandt, Slm lattice structures: Properties, performance, applications and challenges, Mater. Des. 183 (2019) 108137, https://doi.org/10.1016/j.matdes.2019.108137.
[63] M. Dziaduszewska, A. Zieliński, Structural and material determinants influencing the behavior of porous ti and its alloys made by additive manufacturing techniques for biomedical applications, Materials 14 (4) (2021) 712, https://doi.org/10.3390/ma14040712.
[64] O. Al-Ketan, R.K. Abu Al-Rub, Multifunctional mechanical metamaterials based on triply periodic minimal surface lattices, Adv. Eng. Mater. 21 (10) (2019) 1900524, https://doi.org/10.1002/adem.201900524.
[65] U. Gebhardt, T. Gustmann, L. Giebeler, F. Hirsch, J.K. Hufenbach, M. Kästner, Additively manufactured alsi10mg lattices – potential and limits of modelling as-designed structures, Mater. Des. (2022) 110796, https://doi.org/10.1016/j.matdes.2022.110796.
[66] L. Zhang, S. Feih, S. Daynes, S. Chang, M.Y. Wang, J. Wei, W.F. Lu, Energy absorption characteristics of metallic triply periodic minimal surface sheet structures under compressive loading, Addit. Manuf. 23 (2018) 505–515, https://doi.org/10.1016/j.addma.2018.08.007.
[67] M. Bonneric, C. Brugger, N. Saintier, Investigation of the sensitivity of the fatigue resistance to defect position in aluminium alloys obtained by selective laser melting using artificial defects, Int. J. Fatigue 134 (2020) 105505, https://doi.org/10.1016/j.ijfatigue.2020.105505.
[68] Y. Amani, S. Dancette, P. Delroisse, A. Simar, E. Maire, Compression behavior of lattice structures produced by selective laser melting: X-ray tomography based experimental and finite element approaches, Acta Mater. 159 (2018) 395–407, https://doi.org/10.1016/j.actamat.2018.08.030.
[69] A. Raßloff, P. Schulz, R. Kühne, M. Ambati, I. Koch, A.T. Zeuner, M. Gude, M. Zimmermann, M. Kästner, Accessing pore microstructure–property relationships for additively manufactured materials, GAMM-Mitteilungen 44 (4) (2021) e202100012.
[70] M. Dallago, F. Zanini, S. Carmignato, D. Pasini, M. Benedetti, Effect of the geometrical defectiveness on the mechanical properties of slm biomedical ti6al4v lattices, Proc. Struct. Integr. 13 (2018) 161–167, https://doi.org/10.1016/j.prostr.2018.12.027.
[71] M. Dallago, B. Winiarski, F. Zanini, S. Carmignato, M. Benedetti, On the effect of geometrical imperfections and defects on the fatigue strength of cellular lattice structures additively manufactured via selective laser melting, Int. J. Fatigue 124 (2019) 348–360, https://doi.org/10.1016/j.ijfatigue.2019.03.019.
[72] B. Lozanovski, M. Leary, P. Tran, D. Shidid, M. Qian, P. Choong, M. Brandt, Computational modelling of strut defects in slm manufactured lattice structures, Materi. Des. 171 (2019) 107671, https://doi.org/10.1016/j.matdes.2019.107671.
[73] B. Lozanovski, D. Downing, R. Tino, A. du Plessis, P. Tran, J. Jakeman, D. Shidid, C. Emmelmann, M. Qian, P. Choong, et al., Non-destructive simulation of node defects in additively manufactured lattice structures, Addit. Manuf. 36 (2020) 101593, https://doi.org/10.1016/j.addma.2020.101593.
[74] Amtrinsic® spherical ti-42nb powder, https://www.taniobis.com/home/products/productinformations/amtrinsic-spherical-ti-42nb-powder.cc.en.html, accessed: 2022-01-01.
[75] S. Pilz, T. Gustmann, F. Günther, M. Zimmermann, U. Kühn, A. Gebert, Controlling the young's modulus of a ß-type ti-nb alloy via strong texturing by lpbf, Mater. Des. 216 (2022) 110516.
[76] R. Raghava, R.M. Caddell, G.S. Yeh, The macroscopic yield behaviour of polymers, J. Mater. Sci. 8 (2) (1973) 225–232, https://doi.org/10.1007/BF00550671.
[77] R.M. Caddell, R.S. Raghava, A.G. Atkins, Pressure dependent yield criteria for polymers, Mater. Sci. Eng. 13 (2) (1974) 113–120, https://doi.org/10.1016/0025-5416(74)90179-7.
[78] R. Hill, A theory of the yielding and plastic flow of anisotropic metals, Proceedings of the Royal Society of London. Series A. Mathematical and Physical Sciences 193 (1033) (1948) 281–297. doi: 10.1098/rspa.1948.0045.
[79] G.R. Johnson, W.H. Cook, Fracture characteristics of three metals subjected to various strains, strain rates, temperatures and pressures, Eng. Fract. Mech. 21 (1) (1985) 31–48, https://doi.org/10.1016/0013-7944(85)90052-9. URL https://www.sciencedirect.com/science/article/pii/0013794485900529.
[80] C. Schulze, M. Weinmann, C. Schweigel, O. Keßler, R. Bader, Mechanical properties of a newly additive manufactured implant material based on ti-42nb, Materials 11 (1) (2018) 124, https://doi.org/10.3390/ma11010124.
[81] A. Reck, S. Pilz, U. Thormann, V. Alt, A. Gebert, M. Calin, C. Heiß, M. Zimmermann, Effects of thermomechanical history and environment on the fatigue behavior of (β)-ti-nb implant alloys, in: MATEC Web of Conferences, Vol. 165, EDP Sciences, 2018, p. 06001. doi: 10.1051/matecconf/201816506001.
[82] A. Helth, S. Pilz, T. Kirsten, L. Giebeler, J. Freudenberger, M. Calin, J. Eckert, A. Gebert, Effect of thermomechanical processing on the mechanical biofunctionality of a low modulus ti-40nb alloy, J. Mech. Behav. Biomed. Mater. 65 (2017) 137–150, https://doi.org/10.1016/j.jmbbm.2016.08.017.
[83] A. Ataee, Y. Li, M. Brandt, C. Wen, Ultrahigh-strength titanium gyroid scaffolds manufactured by selective laser melting (slm) for bone implant applications, Acta Mater. 158 (2018) 354–368, https://doi.org/10.1016/j.actamat.2018.08.005.
[84] F. Liu, Z. Mao, P. Zhang, D.Z. Zhang, J. Jiang, Z. Ma, Functionally graded porous scaffolds in multiple patterns: New design method, physical and mechanical

properties, Mater. Des. 160 (2018) 849–860, https://doi.org/10.1016/j.matdes.2018.09.053.
[85] C.N. Kelly, T. Wang, J. Crowley, D. Wills, M.H. Pelletier, E.R. Westrick, S.B. Adams, K. Gall, W.R. Walsh, High-strength, porous additively manufactured implants with optimized mechanical osseointegration, Biomaterials 279 (2021) 121206, https://doi.org/10.1016/j.biomaterials.2021.121206.
[86] A. Cheng, D.J. Cohen, A. Kahn, R.M. Clohessy, K. Sahingur, J.B. Newton, S.L. Hyzy, B.D. Boyan, Z. Schwartz, Laser sintered porous ti–6al–4v implants stimulate vertical bone growth, Annals Biomed. Eng. 45 (8) (2017) 2025–2035, https://doi.org/10.1007/s10439-017-1831-7.
[87] F. Calignano, Design optimization of supports for overhanging structures in aluminum and titanium alloys by selective laser melting, Mater. Des. 64 (2014) 203–213, https://doi.org/10.1016/j.matdes.2014.07.043.
[88] D. Wang, Y. Yang, R. Liu, D. Xiao, J. Sun, Study on the designing rules and processability of porous structure based on selective laser melting (slm), J. Mater. Process. Technol. 213 (10) (2013) 1734–1742, https://doi.org/10.1016/j.jmatprotec.2013.05.001.
[89] M. Mazur, M. Leary, S. Sun, M. Vcelka, D. Shidid, M. Brandt, Deformation and failure behaviour of ti-6al-4v lattice structures manufactured by selective laser melting (slm), Int. J. Adv. Manuf. Technol. 84 (5) (2016) 1391–1411, https://doi.org/10.1007/s00170-015-7655-4.
[90] E. Davoodi, H. Montazerian, R. Esmaeilizadeh, A.C. Darabi, A. Rashidi, J. Kadkhodapour, H. Jahed, M. Hoorfar, A.S. Milani, P.S. Weiss, et al., Additively manufactured gradient porous ti–6al–4v hip replacement implants embedded with cell-laden gelatin methacryloyl hydrogels, ACS Appl. Mater. Interfaces 13 (19) (2021) 22110–22123.
[91] V. Karageorgiou, D. Kaplan, Porosity of 3d biomaterial scaffolds and osteogenesis, Biomaterials 26 (27) (2005) 5474–5491, https://doi.org/10.1016/j.biomaterials.2005.02.002.
[92] A. Acciaioli, L. Falco, M. Baleani, Measurement of apparent mechanical properties of trabecular bone tissue: Accuracy and limitation of digital image correlation technique, J. Mech. Behav. Biomed. Mater. 103 (2020) 103542, https://doi.org/10.1016/j.jmbbm.2019.103542.
[93] E. Verhulp, B. van Rietbergen, R. Huiskes, A three-dimensional digital image correlation technique for strain measurements in microstructures, J. Biomech. 37 (9) (2004) 1313–1320, https://doi.org/10.1016/j.jbiomech.2003.12.036.
[94] O. Al-Ketan, D.-W. Lee, R. Rowshan, R.K.A. Al-Rub, Functionally graded and multi-morphology sheet tpms lattices: Design, manufacturing, and mechanical properties, J. Mech. Behav. Biomed. Mater. 102 (2020) 103520, https://doi.org/10.1016/j.jmbbm.2019.103520.
[95] J.C. Hastie, J. Koelblin, M.E. Kartal, M.M. Attallah, R. Martinez, Evolution of internal pores within alsi10mg manufactured by laser powder bed fusion under tension: As-built and heat treated conditions, Mater. Des. 204 (2021) 109645, https://doi.org/10.1016/j.matdes.2021.109645.
[96] Z. Cai, Z. Liu, X. Hu, H. Kuang, J. Zhai, The effect of porosity on the mechanical properties of 3d-printed triply periodic minimal surface (tpms) bioscaffold, Bio-Des. Manuf. 2 (4) (2019) 242–255, https://doi.org/10.1007/s42242-019-00054-7.